nature cell biology

Article

https://doi.org/10.1038/s41556-023-01244-3

Regulators of mitonuclear balance link mitochondrial metabolism to mtDNA expression

Received: 15 February 2023

Accepted: 29 August 2023

Published online: 28 September 2023

Check for updates

Nicholas J. Kramer[1,3], Gyan Prakash[1,3], R. Stefan Isaac[1], Karine Choquet[1], Iliana Soto[1], Boryana Petrova[2], Hope E. Merens[1], Naama Kanarek[2] & L. Stirling Churchman[1]

Mitochondrial oxidative phosphorylation (OXPHOS) complexes are assembled from proteins encoded by both nuclear and mitochondrial DNA. These dual-origin enzymes pose a complex gene regulatory challenge for cells requiring coordinated gene expression across organelles. To identify genes involved in dual-origin protein complex synthesis, we performed fluorescence-activated cell-sorting-based genome-wide screens analysing mutant cells with unbalanced levels of mitochondrial- and nuclear-encoded subunits of Complex IV. We identified genes involved in OXPHOS biogenesis, including two uncharacterized genes: *PREPL* and *NME6*. We found that PREPL specifically impacts Complex IV biogenesis by acting at the intersection of mitochondrial lipid metabolism and protein synthesis, whereas NME6, an uncharacterized nucleoside diphosphate kinase, controls OXPHOS biogenesis through multiple mechanisms reliant on its NDPK domain. Firstly, NME6 forms a complex with RCC1L, which together perform nucleoside diphosphate kinase activity to maintain local mitochondrial pyrimidine triphosphate levels essential for mitochondrial RNA abundance. Secondly, NME6 modulates the activity of mitoribosome regulatory complexes, altering mitoribosome assembly and mitochondrial RNA pseudouridylation. Taken together, we propose that NME6 acts as a link between compartmentalized mitochondrial metabolites and mitochondrial gene expression.

Establishing the mitochondrial proteome requires coordinated gene expression programs across two distinct and physically separated genomes[1–3]. Mitochondria maintain an extrachromosomal genome (mtDNA), which in humans encodes 13 subunits of the oxidative phosphorylation (OXPHOS) complexes—enzymes responsible for cellular energy conversion and aerobic life. The remainder of the OXPHOS complex subunits are encoded in the nucleus, synthesized in the cytosol and imported into mitochondria for proper complex assembly. This gene regulatory challenge is critical for the cell to overcome as dysfunctional mitochondria are implicated in a variety of human diseases, ranging from neurodegeneration to cancer[4–8].

At every stage of mitochondrial gene expression, from mtDNA replication to transcription and translation, the mitochondrial genome is controlled by nuclear-encoded factors[3]. Although the proteins known to control mitochondrial gene expression have expanded in recent years (reviewed in refs. 9,10), a mechanistic understanding of these regulatory pathways, which likely contribute to the co-regulated

[1]Department of Genetics, Blavatnik Institute, Harvard Medical School, Boston, MA, USA. [2]Department of Pathology, Boston Children's Hospital, Harvard Medical School, Boston, MA, USA. [3]These authors contributed equally: Nicholas J. Kramer, Gyan Prakash. e-mail: churchman@genetics.med.harvard.edu

expression of nuclear and mitochondrial-encoded OXPHOS subunits, remains unknown. Nuclear- and mitochondrial-encoded OXPHOS subunits are synthesized in a remarkably balanced manner across a variety of human cell lines[11]. Failure to synthesize the correct stoichiometries of OXPHOS subunits results in 'mitonuclear imbalance', which leads to cellular stress responses[12–16]. In addition, human mitochondria maintain an extensive proteolytic system poised to respond to misassembled OXPHOS subunits[17]. Mitonuclear imbalance caused by disruptions in mitoribosome subunit levels has been implicated in longevity and aging phenotypes in yeast, worms and mice[18–21]. Thus, the establishment and maintenance of a healthy mitochondrial proteome via proper mitocellular communication are critical for cellular physiology.

To identify regulators of mitonuclear balance, we performed fluorescence-activated cell sorting (FACS)-based genome-wide CRISPR (clustered regularly interspaced short palindromic repeats) screens to uncover factors that altered the accumulation of two dual-genome-encoded OXPHOS subunits of Complex IV—COX1 and COX4. Our screens found known regulators of OXPHOS gene regulation and assembly, as well as genes with uncharacterized mitochondrial functions whose depletion led to imbalanced OXPHOS subunit levels. We investigated two poorly characterized genes, *PREPL* and *NME6*, both of which altered Complex IV subunit accumulation but in opposite directions. We found that *PREPL* encodes a dual cytosolic- and mitochondrial-localized protein that is enriched in the brain and functions at the intersection of lipid metabolism and protein synthesis to regulate Complex IV biogenesis. Furthermore, we observed that NME6, an uncharacterized member of the nucleotide diphosphate kinase (NDPK) family, enzymes that catalyse the synthesis of nucleotide triphosphates (NTPs) via phosphate transfer to nucleotide diphosphates (NDPs)[22–24], controls OXPHOS biogenesis through multifaceted mechanisms. We found that NME6, when bound to RCC1L exhibits NDPK activity, which is used to establish mitochondrial pyrimidine triphosphate pools essential for maintaining mitochondrial (mt)-encoded RNA abundance. Moreover, NME6 modulates the activity of mitoribosome regulatory factors, mtRNA pseudouridylation and *MT-CO1* (COX1) transcript stability. Thus, we propose that NME6 is a key enzyme coordinating compartmentalized mitochondrial nucleotide pools with the regulation of mitochondrial gene expression. Together, these screens provide a resource of genes for further avenues of research into mitocellular communication and the regulation of mitochondrial gene expression.

Results

CRISPR screens identify genes regulating mitonuclear balance

To uncover genetic regulators of mitonuclear balance, we designed a FACS-based genome-wide screen to identify factors controlling the levels of OXPHOS subunits destined for the same complex (Complex IV) but encoded by either nuclear or mitochondrial DNA (Fig. 1a). Complex IV assembly, a tightly orchestrated process requiring over 30 assembly factors[25], begins with the synthesis of mitochondrial-encoded *MT-CO1*, which must bind nuclear-encoded *COX4I1* (COX4) to initiate assembly[26]. We found that depleting COX4 with single-guide RNAs (sgRNAs) targeting *COX4I1* led to both the predicted reduction in COX4 and a concurrent reduction in COX1, consistent with COX1 sensing and responding to COX4 levels, as described previously (Fig. 1b,c)[26]. Inhibitors of mitochondrial transcription and translation, ethidium bromide (EtBr) and chloramphenicol (CAP), respectively, reduced the levels of mitochondrial-encoded COX1 but not nuclear-encoded COX4 (Fig. 1b,c). Together, these data established the specificity and dynamic range of our FACS screening conditions and also suggested a directionality to Complex IV biogenesis with mitochondrial gene expression programs poised to respond to nuclear subunit levels.

To perform these screens, we measured endogenous levels of mitochondrial (COX1) and nuclear (COX4) encoded subunits using FACS in K562-Cas9 cells transduced with a genome-wide single guide RNA (sgRNA) library (10 sgRNAs per gene targeting, ~21,000 human nuclear-encoded genes and ~10,000 safe-targeting control sgRNAs; Fig. 1d)[27]. By analysing cells with altered levels of both nuclear- and mitochondrial-derived subunits, as well as cells with disrupted ratios of nuclear/mitochondrial subunits, we disentangled genes generally required for mitochondrial health from genes controlling either specific nuclear or mitochondrial gene expression pathways (Fig. 1e,f, Extended Data Fig. 1a–c).

Our screens revealed known players in mitochondrial biology, as well as many unknown genetic regulators of OXPHOS biogenesis (Fig. 2a, Supplementary Table 1). Positive control sgRNAs targeting *COX4I1* behaved as predicted in our screens, as did genes known to control mitochondrial gene expression at various stages, including mitochondrial transcription (for example, *TFB2M* and *POLRMT*), mtRNA processing (for example, *PDE12* and *FASTKD5*), mitoribosome subunits and translation factors (for example, *TUFM*, *C12ORF65/MTRFR* and *TACO1*) and Complex IV assembly factors (for example, *COA3*, *COA5*, *COA7* and *PET117*). However, many hits were genes with unknown functions in mitochondrial biology, and several had predicted mitochondrial localization in MitoCarta3.0 (ref. 28) (Fig. 2a).

We validated our top hits by infecting cells with individual sgRNAs targeting genes of interest, and measuring COX1, COX4 and ACTB levels by FACS to control for non-specific translation effects (Fig. 2b). Using immunoblots, we confirmed that many hits (44 genes tested) altered COX1, COX4 and ACTB expression in the directions predicted from our FACS screens (Fig. 2c, Extended Data Fig. 2a). We further screened these hits by assessing mitochondrial content (MitoTrackerRed), TFAM levels (as a proxy for mtDNA levels) and Complex V subunit levels to disentangle general mitochondrial regulators from Complex IV specific regulators (Extended Data Fig. 2b,c). We then characterized two top hits with uncharacterized mitochondrial functions, which altered COX1/COX4 ratios in opposite directions: *PREPL* (deletion led to a decreased COX1/COX4 ratio) and *NME6* (deletion led to an increased COX1/COX4 ratio; Fig. 1e,f). We generated homozygous knockout (KO) clones of *PREPL* and *NME6* using CRISPR and confirmed their imbalance phenotypes (Fig. 2d).

Mitochondrial PREPL regulates Complex IV biogenesis

PREPL (prolyl-endopeptidase like) is a human disease gene of unknown function, in which mutations cause congenital myasthenic syndrome[29–34]. *PREPL* deletion in K562 cells caused a reduction in mitochondrial-encoded COX1 whereas nuclear-encoded COX4 remained near wild-type (WT) levels. Reintroduction of cDNA encoding PREPL into *PREPL* KO cells rescued these phenotypes (Fig. 3a). *PREPL* is documented in MitoCarta3.0 (ref. 28); however, we observed that endogenous PREPL is both cytosolic and mitochondrial localized using subcellular cytosolic and mitochondrial fractionation (Fig. 3b). We found two dominant PREPL isoforms expressed in K562 cells—a shorter cytosolic isoform ($PREPL_{(s)}$) and a longer mitochondrial isoform ($PREPL_{(L)}$), consistent with recent observations in HEK293T cells[35]. We verified a mitochondrial matrix localization for $PREPL_{(L)}$ using stimulated emission depletion (STED) superresolution microscopy (Fig. 3d, Extended Data Fig. 3a,b). Furthermore, we observed that PREPL forms a high-molecular-weight species when localized to mitochondria, suggesting that dimerization may contribute to its function (Extended Data Fig. 3d,e). Analysis of various mouse tissues revealed a strong tissue isoform specificity, and high PREPL expression in the brain (Fig. 3c).

Loss of PREPL led to specific reductions in Complex IV levels, including the monomeric, dimeric and supercomplex assemblies, as determined by blue native polyacrylamide gel electrophoresis (BN-PAGE). Furthermore, Seahorse analysis of specific OXPHOS-linked respiratory activity demonstrated Complex IV dysfunction without major Complex I disruption (Fig. 3e–h). Disruptions to Complex IV levels and activity led to basal respiratory defects in PREPL KO cells (Fig. 3i), which were rescued by mitochondrial $PREPL_{(L)}$ expression. To investigate the mechanisms by which PREPL regulates Complex IV

https://doi.org/10.1038/s41556-023-01244-3

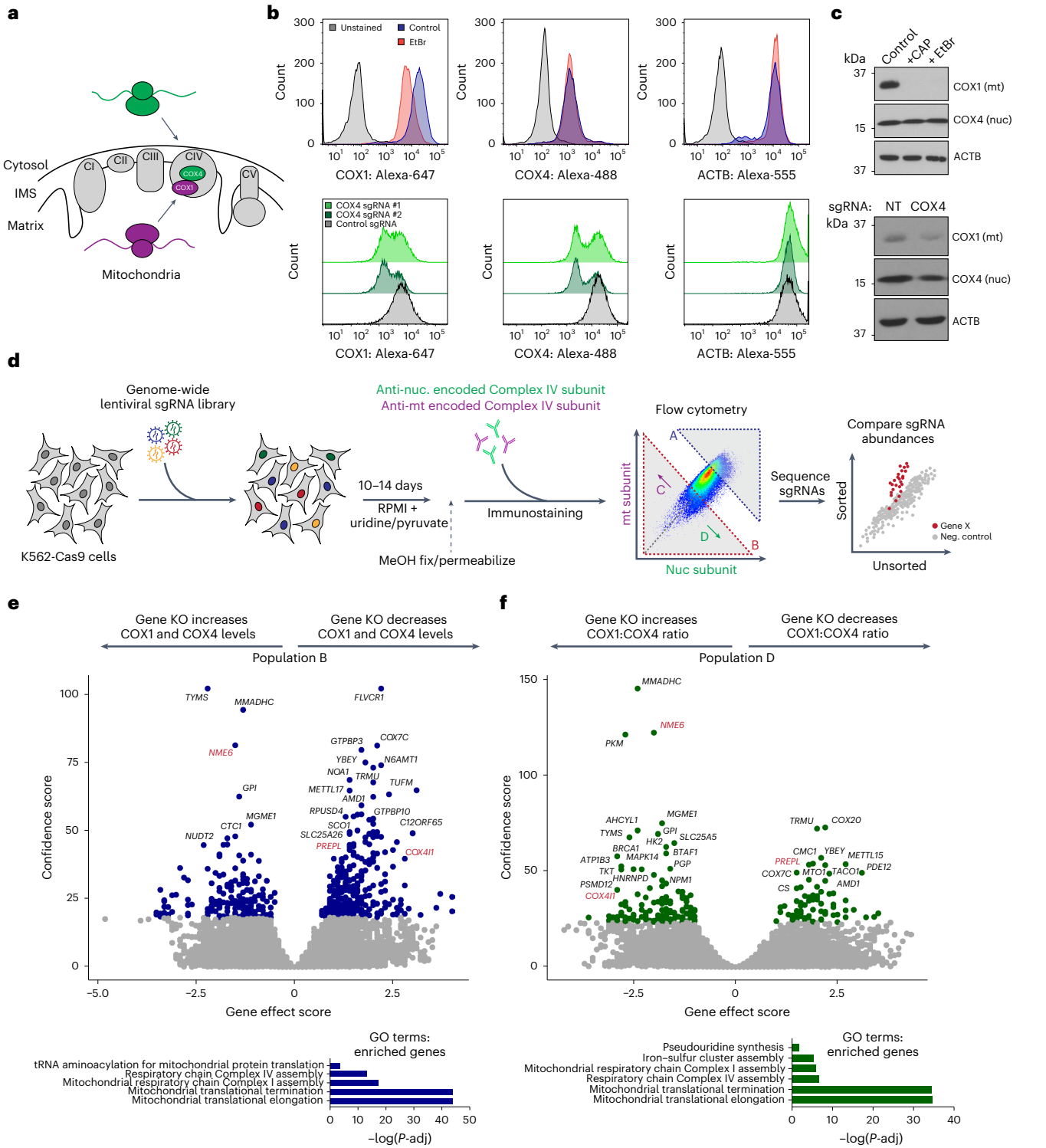

Fig. 1 | Genome-wide CRISPR screens identify regulators of mitonuclear balance. a, Dual-genome-encoded Complex IV biogenesis initiates with synthesis of mito-encoded COX1 and nuclear-encoded COX4. CI–CV, Complexes I–V; IMS, intermembrance space. **b**, FACS immunostaining of COX1, COX4 and ACTB levels after mitochondrial transcriptional inhibition with EtBr (2 μg ml^{-1}, 3 days) or with sgRNAs targeting nuclear-encoded *COX4I1* in K562-Cas9 cells. **c**, Western blot analysis after EtBr treatment (2 μg ml^{-1}, 5 days), CAP treatments (200 μg ml^{-1}, 5 days) or COX4 knock-down (*COX4I1*-targeting sgRNA or non-targeting (NT) control sgRNA). Representative blot of three independently repeated experiments. **d**, Schematic of genome-wide FACS-based CRISPR screening approach to measure mitonuclear subunit expression. The sgRNA libraries include 10 sgRNAs per gene and ~10,000 negative control sgRNAs. Cells were fixed, immunostained and sorted based on expression levels of mito- and nuclear-encoded Complex IV subunits (COX1 and COX4, respectively) after 10–14 days. DNA was purified from sorted (gates A–D) and unsorted control cells to determine sgRNA enrichment or depletion from populations of interest. **e**,**f**, Volcano plots summarizing gene KO effect (enrichment or depletion of sgRNAs in the sorted population relative to unsorted controls) versus confidence scores (blue or green points: hits <10% false-discovery rate (FDR); screens were performed in duplicate, independently; analysed by MAGeCK; Methods). *COX4I1* and hits studied in more detail are shown in red. Significantly enriched gene ontology (GO) terms for positively selected genes (GO biological process, PANTHER: Fisher's exact test with FDR) are shown below. Numerical source data and unprocessed blots are available as source data.

https://doi.org/10.1038/s41556-023-01244-3

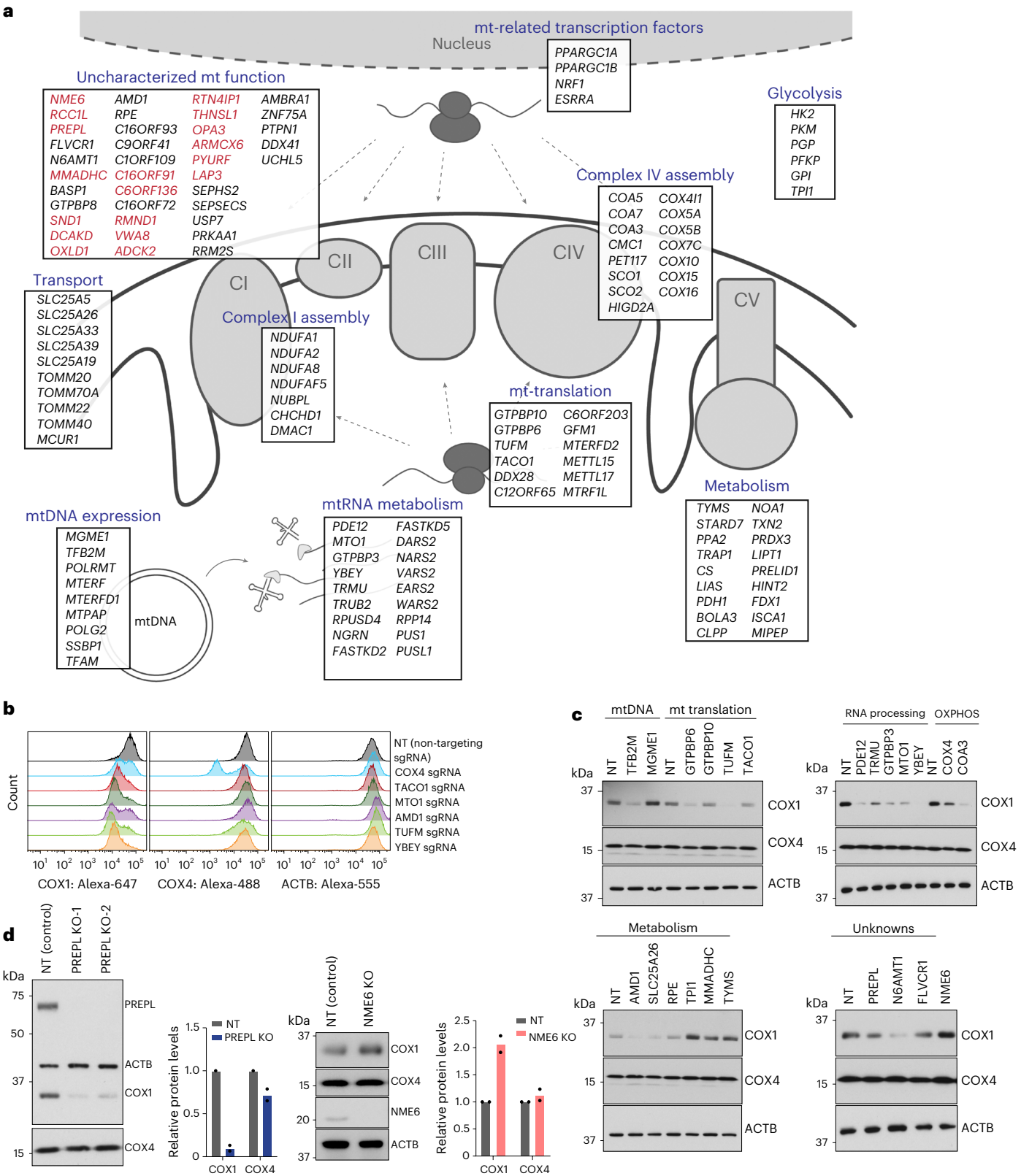

Fig. 2 | Summary of OXPHOS biogenesis regulators identified by CRISPR screens. a, Schematic of selected genes (FDR <10%) grouped by subcellular localization and reported functions. Genes predicted to localize to mitochondria (present in MitoCarta3.0), but with uncharacterized functions in mitochondrial biology are highlighted in red. **b**, FACS validation of individual sgRNAs in methanol-fixed K562 cells, 10 days post-transduction (NT control sgRNA). **c**, Western blot validation of individual sgRNAs, 10 days post-transduction. Representative blot of three independently repeated experiments. **d**, Western blot analysis and quantification of COX1 and COX4 levels in *PREPL* and *NME6* homozygous KO K562 cells (two independently generated clonal KO lines quantified each; normalized to ACTB levels). Numerical source data and unprocessed blots are available as source data.

biogenesis, we identified PREPL$_{(L)}$ protein interactors using immunoprecipitation (IP)–mass spectrometry and found that PREPL$_{(L)}$ interacted with mitochondrial proteins significantly enriched for GO terms, including 'mitochondrial translation' and 'fatty acid beta-oxidation', suggesting a possible link between lipid metabolism and mitoribosome function (Fig. 4a, Extended Data Fig. 4a,b, Supplementary Table 2).

To test the involvement of lipid metabolism in PREPL function, we measured cell proliferation of PREPL KO cells cultured in standard or charcoal-stripped (lipophilic molecule-depleted) serum. We found that PREPL KO cells exhibited decreased proliferation only in charcoal-stripped FBS, suggesting a role for PREPL in lipid utilization (Fig. 4b). A recent study reported thioesterase activity for PREPL in vitro, implicating an active serine residue (S559), as part of a catalytic triad in a putative lipid-binding pocket[35]. By expressing WT or S559A mutant PREPL$_{(L)}$ in PREPL KO cells, we found that S559A-PREPL phenocopied the PREPL KO proliferation defect while WT-PREPL fully restored proliferation levels to those of control cells (Fig. 4b). Moreover, only mitochondrial-localized WT-PREPL$_{(L)}$, but not cytosolic PREPL$_{(s)}$ or S559A mutants, was sufficient to rescue the reduction in COX1 subunit levels (Fig. 4c, Extended Data Fig. 4g). Although we observed small perturbations to mtDNA-encoded OXPHOS subunits in charcoal-stripped media upon PREPL loss, COX1 levels were impacted most severely, with a near complete loss (Extended Data Fig. 4g). Additionally, S559A-PREPL was unable to rescue respiratory defects in PREPL KO cells grown in lipid-depleted media (Fig. 4d). Consistent with its thioesterase activity and the possible lipid binding pocket observed in its structure[35], our data suggest that PREPL is involved in mitochondrial lipid metabolism.

Since GO terms for PREPL protein interactors were also enriched for 'mitochondrial translation', we investigated whether PREPL functions via mitochondrial protein synthesis. Using sucrose gradient ultracentrifugation, we observed that PREPL co-sediments with mitoribosomes, up to the assembled monosome fraction (Fig. 4e, Extended Data Fig. 4c,d). To test the impact on newly synthesized mitochondrial proteins, we performed ^{35}S-methionine labelling. We found that *PREPL* KO specifically reduced COX1 synthesis without major changes in mtDNA levels, mtRNA levels, COX1 RNA processing, poly(A) tail length, COX1 subunit turnover or COX1 translational activator TACO1 levels (Fig. 4f, Extended Data Figs. 3c, 4e,f, 5a,b and 6a–c). Together, our data suggest that PREPL is a brain-enriched, dual cytosolic- and mitochondrial-localized protein that specifically controls Complex IV biogenesis connecting thioesterase activity to the regulation of mitochondrial translation.

NME6 regulates mitochondrial respiration and OXPHOS biogenesis

Our screens predicted that *NME6* mutation disrupts Complex IV subunit ratios by upregulating mitochondrial-encoded COX1—opposite to the *PREPL* deletion. NME6, an uncharacterized nucleoside diphosphate kinase (NDPK), contains a highly conserved histidine within its predicted NDPK domain, residues typically used by NDPK enzymes for phosphate transfer[22] (Fig. 5a). *NME6* is predicted to be an essential gene based on large-scale mouse KO consortia (International Mouse Phenotyping Consortium; MGI:1861676). While NME6 has no predicted mitochondrial targeting sequence, it is included in MitoCarta3.0 (ref. 28). We observed that NME6 localized to the mitochondrial matrix using a combination of confocal microscopy, subcellular fractionations, and proteinase K protection assays (Fig. 5b,c). NME6 loss led to reduced cellular proliferation in the 'physiological' human plasma-like medium (HPLM), consistent with genome-wide screens[36] (Fig. 5d). Reduced proliferation was concurrent with decreased basal and maximal respiration rates (Fig. 5f) and dysregulated OXPHOS subunit levels (Fig. 5e). To test whether these phenotypes relied on the predicted NDPK activity of NME6, we exogenously expressed NME6 with the highly conserved histidine mutated to alanine (H137A), which, in contrast to WT-NME6, was unable to rescue the phenotypes in NME6 KO cells (Fig. 5d,f).

Next, we asked what mechanisms could lead to the proliferation and respiration phenotypes caused by NME6 loss. Because NME6 KO cells had elevated COX1 levels, we tested whether these increased subunits were being integrated into fully assembled complexes and if so, why increased Complex IV levels would lead to respiratory defects. Interestingly, we found that NME6 loss had differential effects across OXPHOS complexes; NME6 KO cells had elevated Complex IV levels but decreased levels of Complex I and III assemblies, leading to reduced supercomplex assemblies. These phenotypes were all reliant on H137A (Fig. 5g). We confirmed the Complex IV upregulation in NME6 KO cells by measuring the Complex IV enzymatic activity *in vitro* from WT and NME6 KO mitochondrial lysates (Fig. 5i, Extended Data Fig. 6d). Furthermore, analysis of OXPHOS complex specific respiratory activity demonstrated disruptions to Complex I activity (Fig. 5h). OXPHOS assembly dysregulation across complexes in NME6 KO cells was further accompanied by defects in mitochondrial cristae morphology (Fig. 5j). Together, NME6 deletion led to disrupted OXPHOS biogenesis and abnormal respiration—phenotypes reliant on a conserved histidine in the NDPK domain of NME6.

NME6 loss disrupts mtRNA abundance

Next, we addressed the mechanism by which NME6 acts to regulate mitochondrial gene expression. To test whether mitochondrial RNA transcripts were affected by NME6 KO, we measured their abundance using a MitoStrings panel[37], which directly measures RNA levels with NanoStrings technologies. These data indicated that the majority of mtRNAs were downregulated in NME6 KO cells, most severely *MT-CYB*, but with the notable exceptions of *MT-RNR1*, *MT-RNR2* and *MT-CO1*, which are more proximal to the heavy strand promoter and were, by contrast, upregulated (Fig. 6a). These changes were not due to alterations in mtDNA copy number (Fig. 6b). The disruptions in mtRNA abundances were consistent with the native OXPHOS complex biogenesis

Fig. 3 | PREPL, a brain-enriched, dual-localized protein, regulates Complex IV biogenesis. a, Representative western blots of COX1 and COX4 subunit levels in NT control sgRNA, PREPL KO, and PREPL KO rescue cells. Representative blot of 3 repeated experiments. **b**, Subcellular fractionation and western blotting for endogenous PREPL or exogenous PREPL$_{(L)}$-Flag. cyto, cytosol fraction; mt, mitochondrial fraction; WC, whole cell. Representative blot of three repeated experiments. **c**, Schematic representation of short and long PREPL protein isoforms and representative western blot detection of PREPL expression and isoform usage across mouse tissues (C57BL/6, 8-week-old males; representative blot of two independently repeated experiments). **d**, Left, representative micrographs of confocal and STED microscopy in U2OS cells transduced with PREPL$_{(L)}$-Flag, immunostained with anti-Flag and anti-TOMM40 (outer mitochondrial membrane marker) antibodies. Right, pixel intensity line scans of fluorescence channels across the indicated dashed line (green, FLAG; magenta, TOMM40 or LRPPRC, matrix marker; Extended Data Fig. 3a for micrograph; scale bars, 10 µm confocal panel, 500 nm STED panels; experiment repeated twice). **e**, BN-PAGE followed by western blot detection (indicated antibody above) of native OXPHOS Complexes I–V. Representative blots of three independent experiments. **f**,**g**, Seahorse extracellular flux assays to measure oxygen consumption rate (OCR) linked to Complex I (**f**) or Complex IV (**g**) in permeabilized K562 cells supplemented with indicated substrates. **h**, Quantification of state 3 respiration defined as the difference between maximal respiratory capacity after addition of substrates specific for Complex I or Complex IV and respiratory capacity after complete inhibition of the respective complex (ns, non-significant; $^{****}P < 0.0001$, $n = 4$ independent cultures, two-way ANOVA with Sidak's multiple comparisons correction, data are means ± s.d.). **i**, Seahorse assay measuring OCR in live cells with mitochondrial stressors (FCCP, carbonyl cyanide-*p*-trifluoromethoxyphenylhydrazone; AA, antimycin A; perm, XF Plasma Membrane Permeabilizer; ADP, adenosine diphosphate; pyr+mal, pyruvate and malate; TMPD/Asc, *N*,*N*,*N*,*N*-tetramethyl-*p*-phenylenediamine/ascorbate; $n = 4$ (control and KO + PREPL) or 5 (PREPL KO) independent cultures). Numerical source data and unprocessed blots are available as source data.

https://doi.org/10.1038/s41556-023-01244-3

defects we observed where Complex IV was upregulated while Complexes I and III were downregulated (Fig. 5g). NME6 KO did not phenocopy the mutation of the transcription initiation factor TFB2M, which showed near equal reduction across all mitochondrial-encoded transcripts (Extended Data Fig. 6e). To test the transcriptional competence of mitochondria lacking NME6, we pulse-labelled purified mitochondria with ^{32}P-UTP (uridine triphosphate) and visualized newly transcribed RNAs with autoradiography (Extended Data Fig. 7a,b). In these bulk measurements, NME6 KO did not cause large-scale changes in the levels of newly synthesized transcripts, indicating that NME6 KO-mediated changes in RNA levels were not due to a broad inhibition of transcriptional machinery.

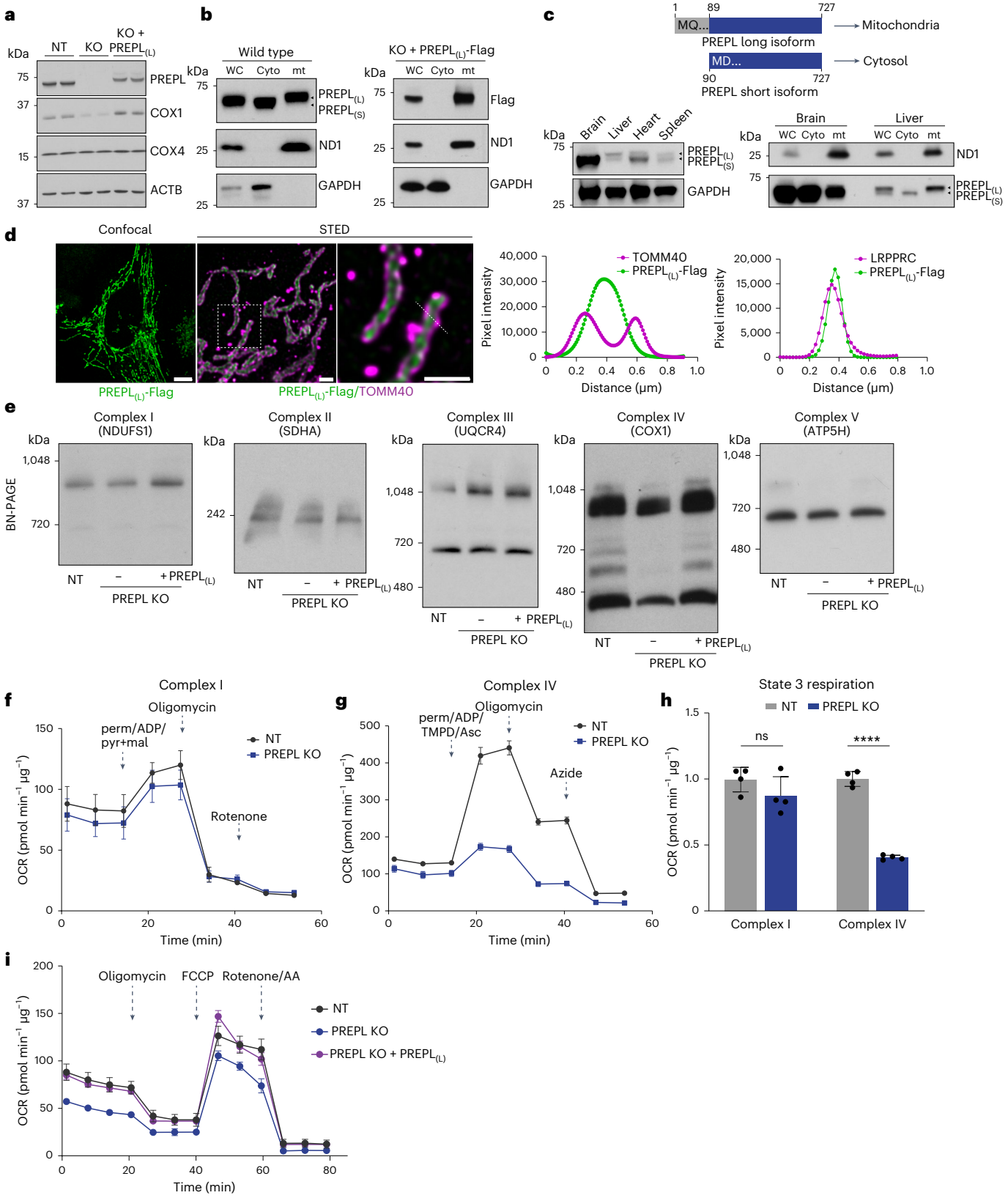

https://doi.org/10.1038/s41556-023-01244-3

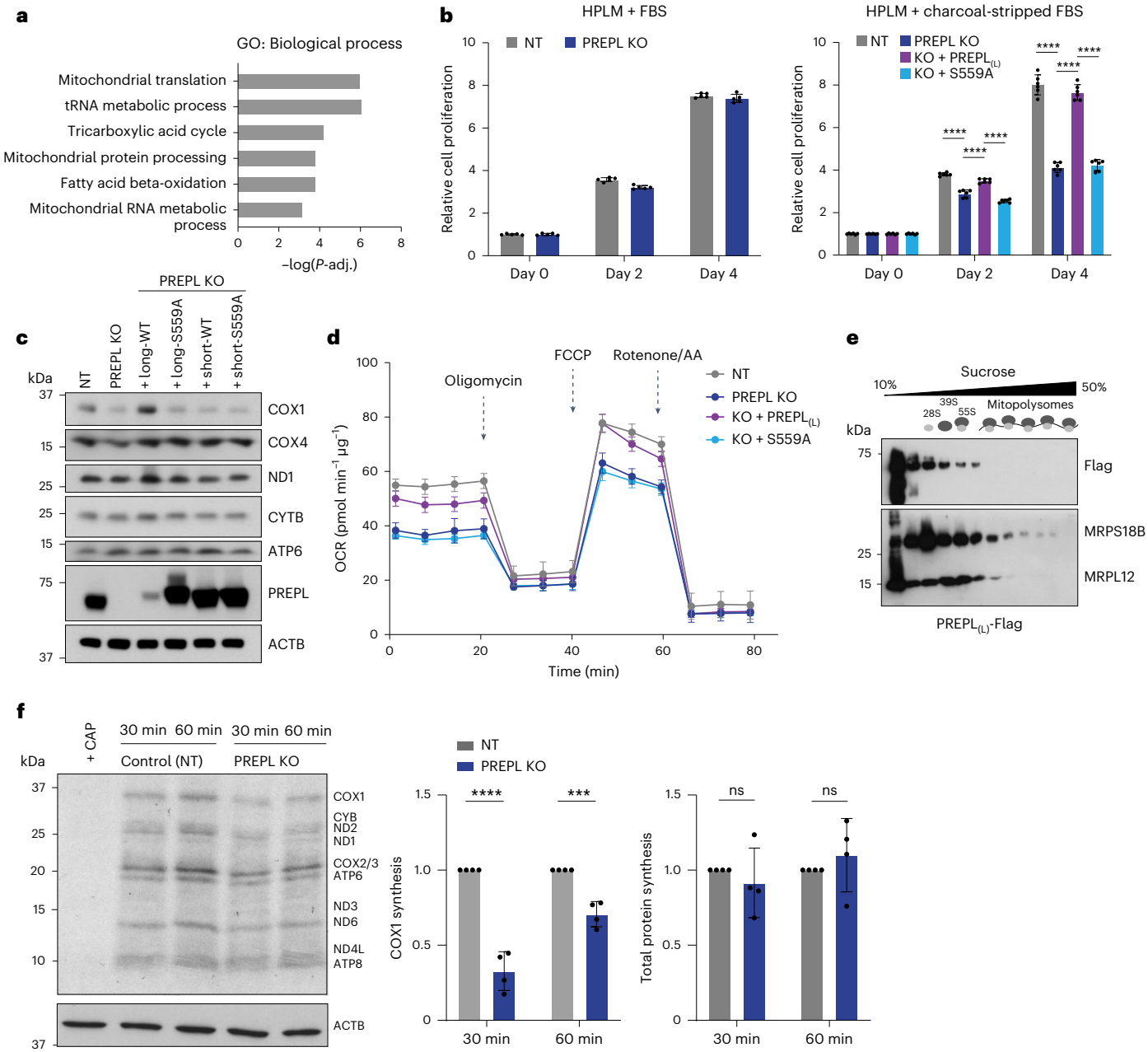

Fig. 4 | PREPL thioesterase activity mediates Complex IV biogenesis. a, GO terms for proteins identified by IP–mass spectrometry and significantly enriched in PREPL$_{(L)}$-Flag IPs relative to control IPs (Panther: GO biological process, Fisher's exact test with FDR). **b**, Cell proliferation measured by CellTiter-Glo in HPLM supplemented with standard FBS (left) or charcoal-stripped FBS (right); S559A = PREPL$_{(L)}$ with serine 559 mutated to alanine (left, $n = 5$ independent cultures; right, $n = 6$ independent cultures, two-way ANOVA with Tukey's multiple comparisons correction, $^{****}P < 0.0001$). **c**, Representative western blot analysis of OXPHOS subunits in control (NT), PREPL KO and KO cells transduced with long or short PREPL isoforms with or without S559A mutation. Experiments repeated twice. **d**, Seahorse assay measuring OCR in live cells grown in HPLM + charcoal-stripped FBS with mitochondrial stressors ($n = 5$ independent cultures). **e**, Western blotting in PREPL-Flag-expressing K562 cells on fractions collected from 10–50% sucrose gradients after ultracentrifugation. Representative blot of two independent experiments. **f**, Left, ^{35}S-methionine metabolic labelling for 30 or 60 min in the presence of anisomycin (100 µg ml^{-1}) followed by autoradiography of mitochondrial translation products and western blotting of ACTB to control for loading. Right, quantification of COX1 synthesis or total protein synthesis (summed intensity of all bands) normalized to loading controls and plotted relative to NT control samples for each gel (CAP, 50 µg ml^{-1}; $n = 4$ independent experiments; Extended Data Fig. 3 for replicate gels, two-way ANOVA with Sidak's multiple comparisons correction, 30 min: $^{****}P < 0.0001$, 60 min: $^{***}P = 0.003$). Data are mean ± s.d. for all plots; ns, non-significant. Numerical source data and unprocessed blots are available as source data.

NME6 establishes mitochondrial pyrimidine pools

As our data implicated the NDPK domain of NME6 for its function, we asked whether NME6 was responsible for maintaining local concentrations of mitochondrial nucleotides. By profiling metabolites using mass spectrometry in whole cell lysates, we observed an accumulation of nucleoside monophosphates, including CMP, UMP and GMP, in NME6 KO cells, suggesting a possible dysregulation of nucleotide biosynthesis; however, only CMP and UMP were dependent on H137A, indicating a role for NME6 specifically in the regulation of pyrimidine levels (Fig. 6c, Extended Data Fig. 8, Supplementary Table 3). Because whole-cell metabolite levels may misrepresent mitochondrial metabolite pools, we analysed mitochondrial-specific metabolite pools using

https://doi.org/10.1038/s41556-023-01244-3

rapid mitochondrial IP (mt-IP)[38]. We found that NME6 KO led to the abnormal mitochondrial accumulation of mono- and diphosphate pyrimidines without disruptions in mono- and diphosphate purine pools or other general metabolite levels (Fig. 6d, Extended Data Fig. 8b–g), indicating a disruption in pyrimidine NTP synthesis in NME6 KO mitochondria. Isotope tracing with ^{13}C-glucose followed by mt-IP and metabolite profiling confirmed disruptions to mitochondrial pyrimidine pools with higher ^{13}C labelling of the pyrimidine mono- and

https://doi.org/10.1038/s41556-023-01244-3

Fig. 5 | Loss of NME6 disrupts OXPHOS biogenesis and mitochondrial respiration. a, Schematic of NDPK family members and protein sequence alignment indicating the highly conserved active-site histidine 137 in NME6 (shading represents level of conservation by percent identity using Clustal Omega NME1–NME2 = 88%, NME1–NME4 = 55%, NME1–NME6 = 25%). **b**, Representative micrographs of U2OS cells transduced with NME6-Flag, immunostained with anti-Flag and anti-LRPPRC antibodies (green, Flag; magenta, LRPPRC; blue, DAPI; scale bars, 10 µm). Experiment repeated twice. **c**, Subcellular fractionation and proteinase K (PK) digestion of mitochondria in the presence or absence of Triton X-100 (TX-100) detergent followed by western blotting with indicated antibodies (KO, NME6 KO). Representative blot of two independently repeated experiments. **d**, Cell proliferation measurements at day 4 relative to day 0 in control (NT) and NME6 KO cells measured by CellTiter-Glo in HPLM ($n = 4$ independent cultures, one-way ANOVA with Tukey's multiple comparisons correction, $^{****}P < 0.0001$). **e**, Representative western blots of COX1, COX4 (Complex IV) and CYTB (Complex III) subunit levels in control (NT), KO and WT/H137A rescue cells. **f**, Seahorse assay assessing OCR in live cells using mitochondrial stressors ($n = 5$ independent cultures). **g**, BN-PAGE followed by western blot detection (indicated antibody above) of native OXPHOS Complexes I–V in control, NME6 KO or KO cells expressing WT- or H137A-NME6. **h**, Seahorse extracellular flux assays to measure OCR in Complex I or IV in permeabilized K562 cells supplemented with indicated substrates (Complex I: $n = 6$ independent cultures; Complex IV: $n = 3$ (NT), $n = 5$ (NME6 KO) independent cultures). **i**, In vitro Complex IV enzymatic activity with indicated mitochondrial lysate amounts ($n = 2$ biological replicate lysates per protein input, experiments were repeated two independent times; lines represent nonlinear fit for the dose–response curves). **j**, Representative electron micrographs of mitochondrial cristae structure by transmission electron microscopy in NT and NME6 KO cells (scale bars, 800 nm (main image) and 116 nm (inset); representative micrograph from 10 field of views). Data are mean ± s.d. Numerical source data and unprocessed blots are available as source data.

diphosphates nucleosides (Extended Data Fig. 8c–f). To determine if disrupted pyrimidine homeostasis was the cause of the perturbed mtRNA abundances and respiratory activity observed in NME6 KO mitochondria, we supplemented NME6 KO cells with uridine for 72 hours (a precursor for pyrimidine NTP biosynthesis). We found that uridine was sufficient to rescue both the altered respiration and downregulated *MT-CYB* mRNA but did not impact upregulated *MT-CO1* mRNA in NME6 KO cells (Fig. 6e,f).

These results suggest that NME6 establishes local pyrimidine NTP levels within mitochondria, which in turn modulates mitochondrial gene expression. Because of the alterations in both steady-state mtRNA abundance and pyrimidine levels in NME6 KO cells, we tested whether UTP incorporation into mitochondrial transcripts was disrupted upon loss of NME6 using 4-thiouridine (4sU) metabolic labelling (Fig. 6g). NME6 KO cells showed reduced 4sU incorporation into all of the mtRNAs measured (the highly stable rRNAs did not pass our statistical cut-off), but not into three control nuclear-encoded RNAs. Taken together, these results suggest that NME6 regulates mtRNA abundance through the establishment of local mitochondrial triphosphate pyrimidine pools.

NME6 interacts with RCC1L to perform NDPK activity

Although we observed disrupted pyrimidine homeostasis in NME6 KO mitochondria, owing to technical limitations, we did not detect measurable NTP levels after mt-IP. Therefore, we tested NDPK activity using recombinant proteins and in vitro NDPK assays. Consistent with previous reports suggesting low NDPK activity by NME6, we were unable to detect ATP hydrolysis, the first step of the NDPK reaction, by NME6 alone[24]. However, NME6 has been reported to interact with the putative guanine exchange factor, RCC1L (WBSCR16), another hit in our screen, which is a poorly characterized protein with connections to mitoribosome assembly[39–41]. Using IP–mass spectrometry, we confirmed that NME6 and RCC1L interact and found that they bind each other with high specificity[42] (Fig. 7a, Supplementary Table 2). Moreover, in a co-IP analysis, we observed that NME6–RCC1L interactions were reduced in H137A-NME6 mutant cells relative to WT-NME6 and that the stability of either protein depended on the presence of the other. Notably, RCC1L knock-down to ~50% of WT levels led to near complete loss of NME6 (Fig. 7b,c, Extended Data Fig. 9a).

When we studied both NME6 and RCC1L using in vitro NDPK assays we found that RCC1L alone hydrolysed ATP (Fig. 7d–h, Extended Data Fig. 8h). We investigated whether NME6 becomes phosphorylated at its conserved histidine via the hydrolysed phosphate by examining NME6 and RCC1L bound in the presence of [γ^{32}P]ATP. We observed phosphorylation of WT-NME6 but not H137A-NME6 or RCC1L (step 2) (Fig. 7f). This phosphate was transferable from NME6 in the presence of acceptor diphosphate nucleotides, forming triphosphate nucleotides, as detected by thin-layer chromatography (TLC; step 3) (Fig. 7g). These data indicate that NME6 and RCC1L function as a heterodimer to perform NDPK activity in mitochondria (Fig. 7h), resolving conflicting data from previous reports[24,39].

NME6 regulates mitoribosome assembly and pseudouridylation

Due to the strong co-dependence of NME6 and RCC1L, we confirmed previous reports that RCC1L interacts with a larger module of mitoribosome-associated proteins that regulate 16S rRNA stability and RNA pseudouridylation levels, including TRUB2, RPUSD4 and RPUSD3 (refs. 43,44) (Extended Data Fig. 10, Supplementary Table 2). We next asked whether NME6 loss altered mitoribosome biogenesis and mtRNA pseudouridylation similar to studies of RCC1L and the associated pseudouridine synthases[40,44]. We found that NME6 co-sediments with mitoribosomes in sucrose gradients and NME6 KO cells showed assembly defects through disruptions of mainly the small mitoribosome subunit (Extended Data Fig. 9b–f). Using CMC-sequencing, NME6 KO cells displayed a ~ 2-fold increase in pseudouridylation at a previously reported modification site within *MT-CO1* mRNA (chrM: 6293), and decreased pseudouridine levels within *MT-TL1* (chrM: 3258). Both modifications were restored to

Fig. 6 | Loss of NME6 regulates mtRNA abundance due to disruption of mitochondrial pyrimidine pools. a, Left, schematic of human mitochondrial DNA. Right, mRNA abundance quantified by MitoStrings (normalized to nuclear-encoded NDUFA7; $P < 0.05$ unless otherwise stated; ns, non-significant; $n = 3$ independent cultures; experiment repeated three times independently). **b**, qPCR measurements of mtDNA levels normalized to nuclear DNA (mitochondrial target, *MT-TL1*; nuclear target, *B2M;* $n = 4$ replicates across two independent experiments). **c**,**d**, Metabolites detected from whole cell (**c**) or mitochondrial-IP (**d**) lysates using liquid chromatography–mass spectrometry (data normalization detailed in Methods; $n = 3$ (whole cell) or 4 (mt-IP) independent cultures per experiment; two-way ANOVA with Dunnett's multiple comparisons correction, $^{*}P = 0.0205$, $^{**}P = 0.0048$, $^{***}P = 0.0008$ (UMP), $^{***}P = 0.0003$ (CDP), $^{****}P < 0.0001$). **e**, Seahorse assay assessing OCR in live cells using mitochondrial stressors in media supplemented with or without uridine ($n = 3$ independent cultures). **f**, qRT-PCR measurements of *MT-CO1* and *MT-CYB* in NT, NME6 KO, KO + NME6-WT cells supplemented with or without uridine (72 h, 50 µg ml^{-1}; $n = 3$ biological replicates, one-way ANOVA with Tukey's multiple comparisons correction). **g**, 4sU transcript incorporation measured by metabolic labelling in control (NT) or NME6 KO cells. Left, schematic of the experimental approach. Right, unlabelled RNAs quantified by MitoStrings (normalized to unlabelled spike-in control; $P < 0.05$ unless otherwise stated, ns = non-significant; $n = 3$ independent cultures, experiment repeated independently twice). Data are mean ± s.d. Numerical source data are available as source data.

https://doi.org/10.1038/s41556-023-01244-3

wild-type levels by WT-NME6 expression (Fig. 8a). NME6 KO did not cause any alteration in the pseudouridine levels in *MT-RNR2* (chrM: 3067), a site previously shown to be regulated by the pseudouridine synthase, RPUSD4, which we confirmed here[43].

Although the function of pseudouridine mRNA modifications is unclear, especially in mitochondria[45,46], they can enhance translation of mRNA-based therapeutics[47–50]. We reasoned that altered *MT-CO1* pseudouridylation levels may impact mRNA stability or translation.

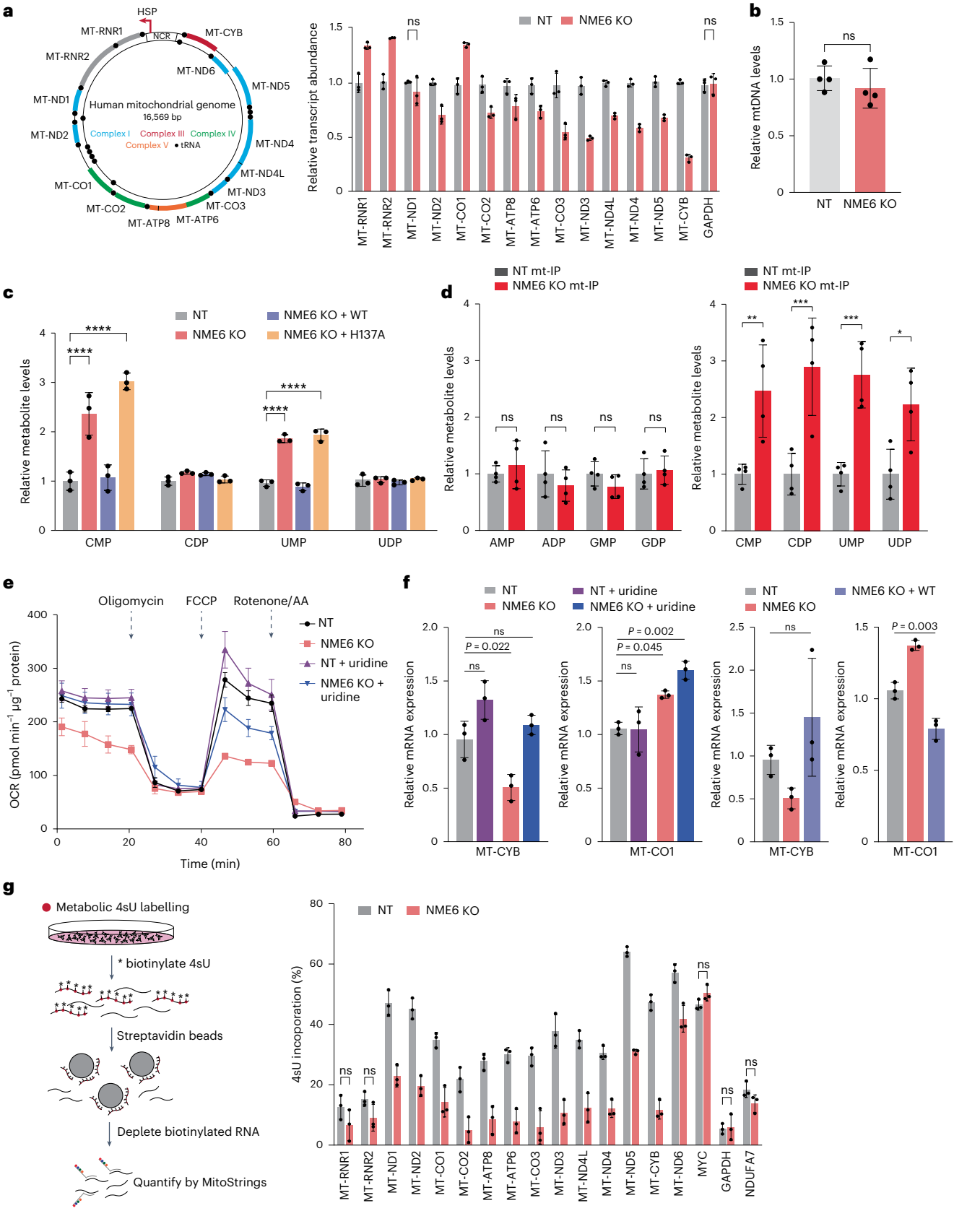

https://doi.org/10.1038/s41556-023-01244-3

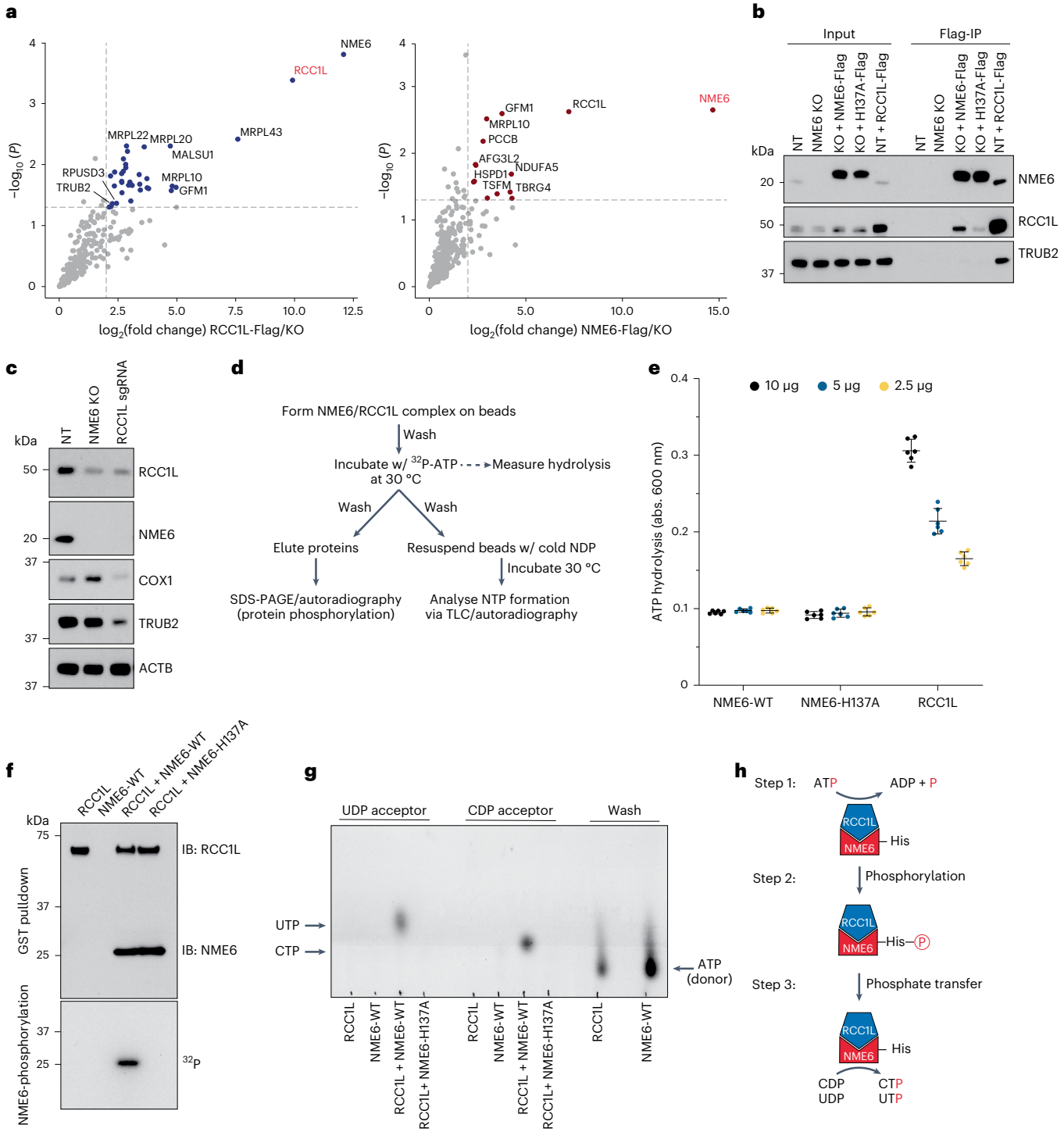

Fig. 7 | NME6 and RCC1L together perform NDPK activity in vitro. a, IP–mass spectrometry identification of proteins interacting with NME6-Flag or RCC1L-Flag in purified mitochondria (coloured points, $P < 0.05$ and $\log_2$(fold change) > 2 indicated by dashed lines, two-tailed Welch's *t*-test). **b**, Co-IP analysis of anti-Flag pull-downs in control (NT), NME6 KO, NME6 KO + WT-NME6-Flag, NME6 KO + H137A-NME6-Flag or NT + RCC1L-Flag cells. Representative blot of three independently repeated experiments. **c**, Western blot analysis of protein levels in NME6 KO cells or RCC1L knock-down cells (RCC1L sgRNA). Representative blot of three independently repeated experiments. **d**, Outline of in vitro assays to test NDPK function using recombinant 6xHis-NME6 (WT or H137A) and GST-RCC1L (TLC, PEI cellulose). **e**, ATP hydrolysis assays with recombinant RCC1L, NME6-WT or NME6-H137A using a malachite green phosphate assay to measure the liberation of free orthophosphate after the addition of ATP (monitored with absorbance at 600 nm ($n = 6$ wells, experiment repeated three independent times; data are mean ± s.d.). **f**, In vitro binding of RCC1L and NME6 using glutathione agarose bead pull-downs and immunoblotting with indicated antibodies (top) and (bottom) protein phosphorylation analysis using SDS-PAGE and autoradiography after incubation with γ-^{32}P ATP. Representative blot of three independently repeated experiments. **g**, TLC (PEI-cellulose plates, 1.2 M LiCl solvent) analysis of NTP formation using autoradiography. Cold UDP or cold CDP were used as acceptor nucleotides for phosphate transfer reactions (representative TLC plate from three independent experiments). **h**, Model of NDPK activity by NME6/RCC1L. Briefly, RCC1L is required for initial ATP hydrolysis (step 1), NME6 is phosphorylated at H137 (step 2) and phosphate is transferred from NME6-H137 to acceptor diphosphate nucleosides (step 3). Numerical source numerical data and unprocessed blots are available as source data.

https://doi.org/10.1038/s41556-023-01244-3

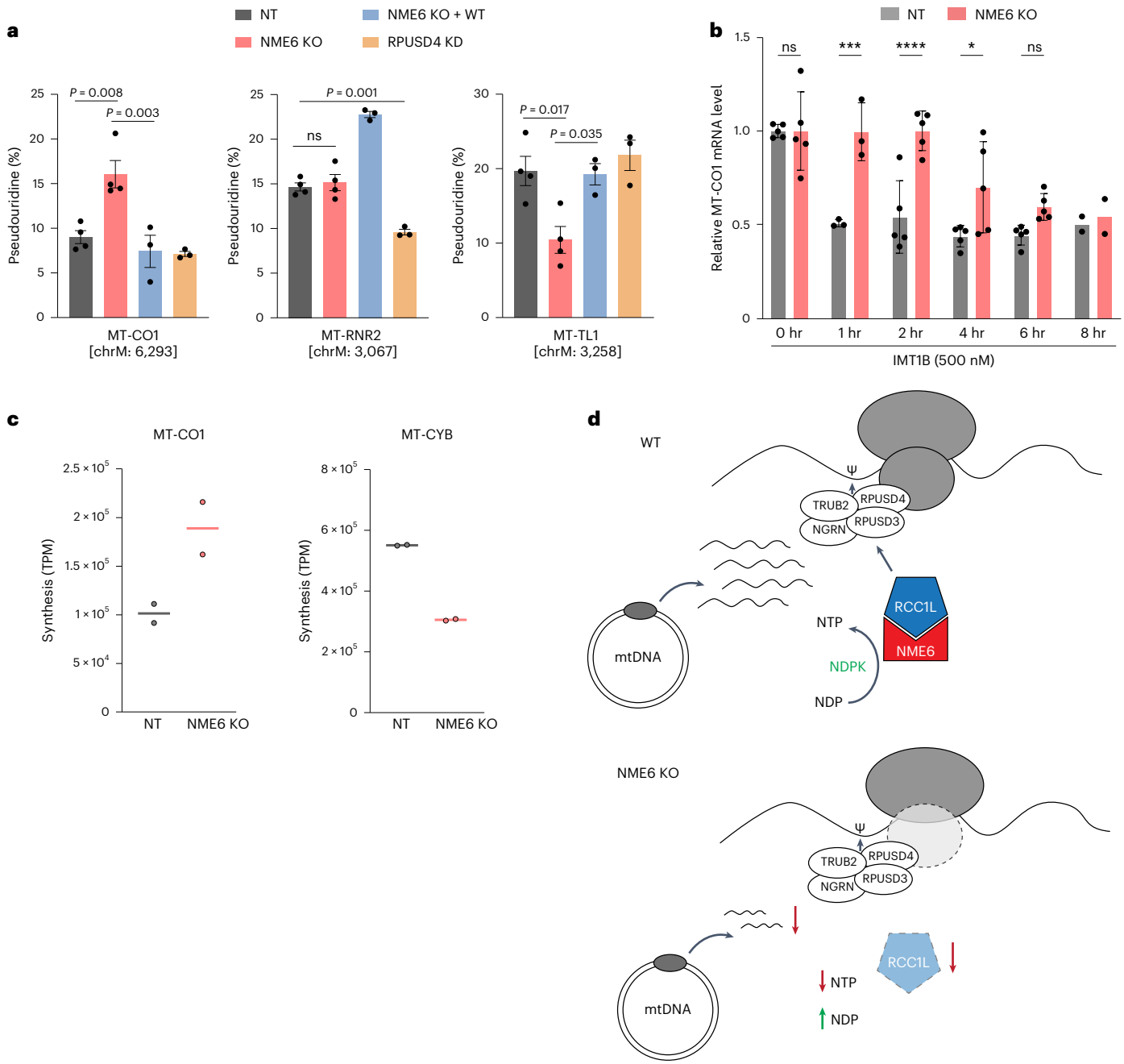

Fig. 8 | NME6 KO disrupts mtRNA pseudouridylation levels increasing *MT-CO1* RNA stability and synthesis. a, CMC-sequencing of NT, NME6 KO, KO + NME6-WT and RPUSD4 knock-down (KD) cells to measure pseudouridine levels at three high-confidence modification sites in *MT-CO1*, *RNR2* and *MT-TL* ($n = 3$ (KO + NME6-WT, RPUSD4 KD) or 4 (NT, NME6 KO) biological replicates across three independent sequencing experiments and two independently generated clonal KO cell lines for *NME6*, one-way ANOVA with Tukey's multiple comparisons corrections). **b**, qRT-PCR measurements of *MT-CO1* mRNA levels after treatment with IMT1B (500 nM) for indicated time in NT or NME6 KO K562 cells (data normalized to ACTB and plotted relative to 0 hr levels; n = 5 (0 hr, 2 hr, 4 hr, 6 hr), 3 (1 hr) or 2 (8 hr) independent cultures from 2 independent experiments; $^{*}P = 0.029$, $^{***}P = 0.0006$, $^{****}P < 0.0001$; two-way ANOVA with Sidak's multiple comparisons correction). **c**, Ribosome profiling analysis plotting synthesis representing mitoribosome protected footprints mapped to *MT-CO1* or *MT-CYB* ($n = 2$ independent sequencing experiments). **d**, Schematic of NME6 function linking local mitochondrial metabolites to the regulation of mitochondrial gene expression. NME6 functions as a heterodimer with RCC1L which together perform NDPK activity to regulate mitochondrial pyrimidine levels. Upon deletion of NME6, mitochondrial pyrimidine homeostasis is disrupted leading to decreased levels of most mtRNAs, with the exception of *MT-CO1*. NME6/RCC1L further interact with mitoribosome associated assembly factors and alter the activity of pseudouridine synthases (Ψ, pseudouridine modified base). Bar plots all represent mean ± s.d. Numerical source data are available as source data.

After inhibiting the mtRNA synthesis with the specific inhibitor, IMT1B, we observed increased *MT-CO1* mRNA stability in NME6 KO cells (Fig. 8b)[51]. Furthermore, *MT-CO1* mRNA had a higher mitoribosome occupancy compared with control cells, indicating that greater *MT-CO1* stability leads to increased synthesis and greater COX1 protein levels (Fig. 8c). On the other hand, transcripts downregulated in NME6 KO, such as *MT-CYB*, showed lower mitoribosome occupancy (Fig. 8c, Extended Data Fig. 7c). Thus, in complex with RCC1L, NME6 regulates mitochondrial nucleotide levels, mitoribosome biogenesis and mtRNA abundances (Fig. 8d).

Discussion

Here, we performed genome-wide screens to find regulators of mitonuclear balance. In addition to well-established OXPHOS regulators, among our top-ranked hits were several genes with uncharacterized functions in mitochondria. Thus, we believe these screens provide a high-quality resource for investigating OXPHOS biogenesis. We focus on two genes here, *PREPL* and *NME6*, out of the many we predict to regulate OXPHOS biogenesis. We found that both PREPL and NME6 connect mitochondrial metabolism to mtDNA expression, highlighting the potential of mitochondrial gene expression to respond to the local metabolic state.

Analysis of mutants with both increased and decreased OXPHOS subunit abundances allowed us to uncover positive and negative regulators of Complex IV biogenesis. These results are complementary to cell death or growth screens with OXPHOS inhibitors to uncover OXPHOS regulators[44,52]. The majority of our hits impacted levels of mitochondrial-encoded COX1 more so than nuclear-encoded COX4, suggesting that mitochondrial gene expression is dynamic and prone to multiple sources of regulation, a phenomenon also observed recently in genome-scale Perturb-seq studies[53].

PREPL, encodes a putative oligoserine peptidase and mutations in *PREPL* cause congenital myasthenic syndrome 22 (CMS22; Online Mendelian Inheritance in Man (OMIM): 616224)[30], a recessive disorder characterized by neuromuscular transmission defects, neonatal hypotonia, and growth hormone deficiencies. Whereas *PREPL* KO mice exhibit growth and hypotonia phenotypes[54], the molecular mechanisms of PREPL function remain elusive and peptide substrates have not been identified[55,56]. We found that within the mitochondrial matrix, $PREPL_{(L)}$ associates with protein synthesis machinery leading to defects in COX1 synthesis. Furthermore, PREPL phenotypes were dependent on a serine residue previously implicated in thioesterase function in vitro[35]. Our data now establish the importance of PREPL thioesterase activity in human mitochondria suggesting that PREPL functions at the interface of lipid metabolism and mitoribosome function. Various mitochondrial fatty acid synthesis pathways impact OXPHOS biogenesis and assembly within the mitochondrial inner membrane. For example, thioester linkages formed through the conserved serine residues of mitochondrial acyl carrier proteins regulate the biogenesis of specific OXPHOS complexes in yeast and human cells[57,58]. Considering that PREPL has thioesterase activity and co-sediments with the mitoribosome, we speculate that PREPL functions to regulate the co-translational membrane insertion of COX1, and, in turn, Complex IV biogenesis.

We observed tissue specificity of PREPL expression and isoform usage with an enrichment of PREPL in the brain, consistent with its genetic involvement in CMS22. In a global analysis, PREPL interacted with the mitoribosome in a tissue-specific manner[59]. Understanding the tissue specificity and function of the PREPL isoforms will illuminate the function of PREPL in both physiology and disease.

Next, we characterized *NME6*, a gene that, when mutated, led to the increased mitochondrial-encoded COX1. Our data show that NME6 is mitochondrially localized and plays a key role in regulating mitochondrial gene expression through its conserved NDPK domain. Despite respiratory and proliferation phenotypes, *NME6* KO did not simply lead to general reductions in OXPHOS biogenesis. But rather, NME6 is involved in multifaceted OXPHOS gene regulation playing differential roles across each complex.

NME6 KO cells had decreased levels of most mt-mRNAs, with pronounced exceptions (*MT-RNR1, MT-RNR2* and *MT-CO1*). While NME6-deficient mitochondria remained broadly transcriptionally competent, our transcriptomics and metabolomics data indicate that NME6 regulates mitochondrial pyrimidine homeostasis via its NDPK domain, consistent with a recent study[60]. NME6 binds specifically to RCC1L and their stabilities rely on the presence of one another, suggesting they exist as an obligate heterodimer. Furthermore, NME6 functions as a NDPK enzyme, but it requires ATP hydrolysis by RCC1L to receive and transfer phosphate groups to an acceptor NDP—a distinct mechanism compared with canonical NPDK enzymes[61]. However, this role is insufficient to explain the upregulated *MT-CO1* mtRNA abundance in NME6 KO cells.

To this end, we identified a second function for NME6 through RCC1L, which interacts with several mitochondrial pseudouridine synthases associated with the mitoribosome[43,44]. Consistently, NME6 KO cells have increased mtRNA pseudouridylation, particularly within *MT-CO1* mRNA, which we hypothesize upregulates *MT-CO1* transcript levels through mRNA stabilization, resulting in higher COX1 synthesis in NME6 KO cells.

Together, our data suggest that NME6 has multifaceted functions in mitochondrial gene regulation, including the regulation of mitochondrial pyrimidine nucleotide pools through its NDPK activity, and the regulation of mitochondrial ribosome assembly, and mtRNA pseudouridylation. Considering these functions and its activity-dependent stability, we propose that NME6–RCC1L acts as a metabolic sensor to tune mitochondrial gene expression based on compartmentalized metabolite availability in the mitochondria. Metabolite compartmentalization is emerging as a key mechanism underlying important physiological processes, such as proline biosynthesis and mammalian development[62–65]. Interestingly, *NME6* is an essential gene for diffuse midline glioma cancer cell growth, a cancer with a selective dependency on pyrimidine biogenesis[66]. In future work, it will be important to determine which NME6 roles contribute to its essentiality and whether its potential role as a metabolic sensor contributes to interorganellar communication to drive cellular transitions in response to environmental cues.

Online content

Any methods, additional references, Nature Portfolio reporting summaries, source data, extended data, supplementary information, acknowledgements, peer review information; details of author contributions and competing interests; and statements of data and code availability are available at https://doi.org/10.1038/s41556-023-01244-3.

References

1. Ryan, M. T. & Hoogenraad, N. J. Mitochondrial-nuclear communications. *Annu. Rev. Biochem.* **76**, 701–722 (2007).
2. Mottis, A., Herzig, S. & Auwerx, J. Mitocellular communication: shaping health and disease. *Science* **366**, 827–832 (2019).
3. Isaac, R. S., McShane, E. & Churchman, L. S. The multiple levels of mitonuclear coregulation. *Annu. Rev. Genet.* **52**, 511–533 (2018).
4. Chan, D. C. Mitochondria: dynamic organelles in disease, aging, and development. *Cell* **125**, 1241–1252 (2006).
5. Wallace, D. C. A mitochondrial paradigm of metabolic and degenerative diseases, aging, and cancer: a dawn for evolutionary medicine. *Annu. Rev. Genet.* **39**, 359–407 (2005).
6. Suomalainen, A. & Battersby, B. J. Mitochondrial diseases: the contribution of organelle stress responses to pathology. *Nat. Rev. Mol. Cell Biol.* **19**, 77–92 (2018).
7. Vafai, S. B. & Mootha, V. K. Mitochondrial disorders as windows into an ancient organelle. *Nature* **491**, 374–383 (2012).
8. Nunnari, J. & Suomalainen, A. Mitochondria: in sickness and in health. *Cell* **148**, 1145–1159 (2012).
9. Rackham, O. & Filipovska, A. Organization and expression of the mammalian mitochondrial genome. *Nat. Rev. Genet.* **23**, 606–623 (2022).
10. Kummer, E. & Ban, N. Mechanisms and regulation of protein synthesis in mitochondria. *Nat. Rev. Mol. Cell Biol.* **22**, 307–325 (2021).
11. Soto, I. et al. Balanced mitochondrial and cytosolic translatomes underlie the biogenesis of human respiratory complexes. *Genome Biol.* **23**, 170 (2022).
12. Kujoth, G. C. et al. Mitochondrial DNA mutations, oxidative stress, and apoptosis in mammalian aging. *Science* **309**, 481–484 (2005).

13. Gomes, A. P. et al. Declining NAD^+ induces a pseudohypoxic state disrupting nuclear-mitochondrial communication during aging. *Cell* **155**, 1624–1638 (2013).
14. Molenaars, M., Daniels, E. G., Meurs, A., Janssens, G. E. & Houtkooper, R. H. Mitochondrial cross-compartmental signalling to maintain proteostasis and longevity. *Philos. Trans. R. Soc. Lond. B* **375**, 20190414 (2020).
15. Haynes, C. M. & Ron, D. The mitochondrial UPR – protecting organelle protein homeostasis. *J. Cell Sci.* **123**, 3849–3855 (2010).
16. Sutandy, F. X. R., Gößner, I., Tascher, G. & Münch, C. A cytosolic surveillance mechanism activates the mitochondrial UPR. *Nature* **618**, 849–854 (2023).
17. Szczepanowska, K. & Trifunovic, A. Tune instead of destroy: how proteolysis keeps OXPHOS in shape. *Biochim. Biophys. Acta Bioenerg.* **1862**, 148365 (2021).
18. Houtkooper, R. H. et al. Mitonuclear protein imbalance as a conserved longevity mechanism. *Nature* **497**, 451–457 (2013).
19. Heeren, G. et al. The mitochondrial ribosomal protein of the large subunit, Afo1p, determines cellular longevity through mitochondrial back-signaling via TOR1. *Aging* **1**, 622–636 (2009).
20. Delaney, J. R. et al. Stress profiling of longevity mutants identifies Afg3 as a mitochondrial determinant of cytoplasmic mRNA translation and aging. *Aging Cell* **12**, 156–166 (2013).
21. Caballero, A. et al. Absence of mitochondrial translation control proteins extends life span by activating sirtuin-dependent silencing. *Mol. Cell* **42**, 390–400 (2011).
22. Boissan, M., Schlattner, U. & Lacombe, M.-L. The NDPK/NME superfamily: state of the art. *Lab Invest.* **98**, 164–174 (2018).
23. Mehus, J. G., Deloukas, P. & Lambeth, D. O. NME6: a new member of the nm23/nucleoside diphosphate kinase gene family located on human chromosome 3p21.3. *Hum. Genet.* **104**, 454–459 (1999).
24. Tsuiki, H. et al. A novel human nucleoside diphosphate (NDP) kinase, Nm23-H6, localizes in mitochondria and affects cytokinesis. *J. Cell. Biochem.* **76**, 254–269 (1999).
25. Signes, A. & Fernandez-Vizarra, E. Assembly of mammalian oxidative phosphorylation complexes I-V and supercomplexes. *Essays Biochem.* **62**, 255–270 (2018).
26. Richter-Dennerlein, R. et al. Mitochondrial protein synthesis adapts to influx of nuclear-encoded protein. *Cell* **167**, 471–483. e10 (2016).
27. Morgens, D. W. et al. Genome-scale measurement of off-target activity using Cas9 toxicity in high-throughput screens. *Nat. Commun.* **8**, 15178 (2017).
28. Rath, S. et al. MitoCarta3.0: an updated mitochondrial proteome now with sub-organelle localization and pathway annotations. *Nucleic Acids Res.* **49**, D1541–D1547 (2021).
29. Jaeken, J. et al. Deletion of PREPL, a gene encoding a putative serine oligopeptidase, in patients with hypotonia-cystinuria syndrome. *Am. J. Hum. Genet.* **78**, 38–51 (2006).
30. Régal, L. et al. PREPL deficiency with or without cystinuria causes a novel myasthenic syndrome. *Neurology* **82**, 1254–1260 (2014).
31. Régal, L. et al. PREPL deficiency: delineation of the phenotype and development of a functional blood assay. *Genet. Med.* **20**, 109–118 (2018).
32. Chabrol, B. et al. Deletion of *C2orf34*, *PREPL* and *SLC3A1* causes atypical hypotonia–cystinuria syndrome. *BMJ Case Rep.* **2009**, bcr0820080719 (2009).
33. Yang, Q. et al. PREPL deficiency: a homozygous splice site PREPL mutation in a patient with congenital myasthenic syndrome and absence of ovaries and hypoplasia of uterus. *Front. Genet.* **11**, 198 (2020).
34. Parvari, R. et al. A recessive contiguous gene deletion of chromosome 2p16 associated with cystinuria and a mitochondrial disease. *Am. J. Hum. Genet.* **69**, 869–875 (2001).
35. Rosier, K. et al. Prolyl endopeptidase-like is a (thio)esterase involved in mitochondrial respiratory chain function. *iScience* **24**, 103460 (2021).
36. Rossiter, N. J. et al. CRISPR screens in physiologic medium reveal conditionally essential genes in human cells. *Cell Metab.* **33**, 1248–1263.e9 (2021).
37. Wolf, A. R. & Mootha, V. K. Functional genomic analysis of human mitochondrial RNA processing. *Cell Rep.* **7**, 918–931 (2014).
38. Chen, W. W., Freinkman, E. & Sabatini, D. M. Rapid immunopurification of mitochondria for metabolite profiling and absolute quantification of matrix metabolites. *Nat. Protoc.* **12**, 2215–2231 (2017).
39. Proust, B. et al. NME6 is a phosphotransfer-inactive, monomeric NME/NDPK family member and functions in complexes at the interface of mitochondrial inner membrane and matrix. *Cell Biosci.* **11**, 195 (2021).
40. Reyes, A., Favia, P., Vidoni, S., Petruzzella, V. & Zeviani, M. RCC1L (WBSCR16) isoforms coordinate mitochondrial ribosome assembly through their interaction with GTPases. *PLoS Genet.* **16**, e1008923 (2020).
41. Huang, G. et al. WBSCR16 Is a guanine nucleotide exchange factor important for mitochondrial fusion. *Cell Rep.* **20**, 923–934 (2017).
42. Antonicka, H. et al. A high-density human mitochondrial proximity interaction network. *Cell Metab.* **32**, 479–497.e9 (2020).
43. Antonicka, H. et al. A pseudouridine synthase module is essential for mitochondrial protein synthesis and cell viability. *EMBO Rep.* **18**, 28–38 (2017).
44. Arroyo, J. D. et al. A genome-wide CRISPR death screen identifies genes essential for oxidative phosphorylation. *Cell Metab.* **24**, 875–885 (2016).
45. Dai, Q. et al. Quantitative sequencing using BID-seq uncovers abundant pseudouridines in mammalian mRNA at base resolution. *Nat. Biotechnol.* **41**, 344–354 (2022).
46. Martinez, N. M. et al. Pseudouridine synthases modify human pre-mRNA co-transcriptionally and affect pre-mRNA processing. *Mol. Cell* **82**, 645–659.e9 (2022).
47. Svitkin, Y. V. et al. N1-methyl-pseudouridine in mRNA enhances translation through eIF2α-dependent and independent mechanisms by increasing ribosome density. *Nucleic Acids Res.* **45**, 6023–6036 (2017).
48. Svitkin, Y. V., Gingras, A.-C. & Sonenberg, N. Membrane-dependent relief of translation elongation arrest on pseudouridine- and N1-methyl-pseudouridine-modified mRNAs. *Nucleic Acids Res.* **22**, 7202–7215 (2021).
49. Nance, K. D. & Meier, J. L. Modifications in an emergency: the role of N1-methylpseudouridine in COVID-19 vaccines. *ACS Cent. Sci.* **7**, 748–756 (2021).
50. Kim, K. Q. et al. N1-methylpseudouridine found within COVID-19 mRNA vaccines produces faithful protein products. *Cell Rep.* **40**, 111300 (2022).
51. Bonekamp, N. A. et al. Small-molecule inhibitors of human mitochondrial DNA transcription. *Nature* **588**, 712–716 (2020).
52. To, T.-L. et al. A compendium of genetic modifiers of mitochondrial dysfunction reveals intra-organelle buffering. *Cell* **179**, 1222–1238.e17 (2019).
53. Replogle, J. M. et al. Mapping information-rich genotype-phenotype landscapes with genome-scale Perturb-seq. *Cell* **185**, 2559–2575.e28 (2022).
54. Lone, A. M. et al. Deletion of PREPL causes growth impairment and hypotonia in mice. *PLoS One* **9**, e89160 (2014).
55. Martens, K. et al. PREPL: a putative novel oligopeptidase propelled into the limelight. *Biol. Chem.* **387**, 879–883 (2006).

56. Szeltner, Z., Alshafee, I., Juhász, T., Parvari, R. & Polgár, L. The PREPL A protein, a new member of the prolyl oligopeptidase family, lacking catalytic activity. *Cell. Mol. Life Sci.* **62**, 2376–2381 (2005).
57. Tang, J. X., Thompson, K., Taylor, R. W. & Oláhová, M. Mitochondrial OXPHOS biogenesis: co-regulation of protein synthesis, import, and assembly pathways. *Int. J. Mol. Sci.* **21**, 3820 (2020).
58. Van Vranken, J. G. et al. ACP acylation is an acetyl-CoA-dependent modification required for electron transport chain assembly. *Mol. Cell* **71**, 567–580.e4 (2018).
59. Busch, J. D. et al. MitoRibo-Tag mice provide a tool for in vivo studies of mitoribosome composition. *Cell Rep.* **29**, 1728–1738.e9 (2019).
60. Grotehans, N. et al. Ribonucleotide synthesis by NME6 fuels mitochondrial gene expression. *EMBO J.* **13**, e113256 (2023).
61. Schlattner, U. The complex functions of the NME family-a matter of location and molecular activity. *Int. J. Mol. Sci.* **22**, 13083 (2021).
62. Bar-Peled, L. & Kory, N. Principles and functions of metabolic compartmentalization. *Nat. Metab.* **4**, 1232–1244 (2022).
63. Solmonson, A. et al. Compartmentalized metabolism supports midgestation mammalian development. *Nature* **604**, 349–353 (2022).
64. Zhu, J. et al. Mitochondrial NADP(H) generation is essential for proline biosynthesis. *Science* **372**, 968–972 (2021).
65. Tran, D. H. et al. Mitochondrial NADP+ is essential for proline biosynthesis during cell growth. *Nat. Metab.* **3**, 571–585 (2021).
66. Pal, S. et al. A druggable addiction to de novo pyrimidine biosynthesis in diffuse midline glioma. *Cancer Cell* **40**, 957–972. e10 (2022).

Methods

All research methods comply with ethical guidelines approved by Harvard University's Committee on Microbial Safety and approved IACUC protocols.

Cell culture

K562 cells were grown in RPMI-1640 medium with GlutaMAX (Thermo Fisher Scientific), 10% standard FBS or 10% charcoal-stripped FBS, where noted (Thermo Fisher Scientific), penicillin (10,000 IU ml^{-1}), and streptomycin (10,000 µg ml^{-1}). Cells used for CRISPR-Cas9 screens were cultured without penicillin or streptomycin, and were supplemented with uridine (50 µg ml^{-1}) and sodium pyruvate (1 mM) to maintain mutant cells with dysfunctional mitochondria. Cells were maintained in a 37 °C humidified incubator with 5% CO_2. HEK293T and U2OS cells were cultured in DMEM with 10% FBS, penicillin (10,000 IU ml^{-1}), and streptomycin (10,000 µg ml^{-1}) in a 37 °C humidified incubator with 5% CO_2. All cell lines were obtained from ATCC (K562: CCL-243, HEK293T: CRL-3216, U2OS: HTB-96).

Mouse strains

8-week-old male C57BL/6 (Charles River, C57BL/6NCrl) mice were used for tissue collection where indicated.

Lentivirus packaging and transductions

Lentivirus were packaged in HEK293T cells following standard protocols for third-generation packaging. Lentivirus-containing medium was harvested 48 hours post-transfection of HEK293T cells and filtered using 0.45 µm PES membranes or centrifuged for 5 minutes at 300*g* to remove cellular debris. K562 cells were transduced with lentiviral media using spin-infection methods. Filtered lentiviral supernatants were added to K562 cells with 8 µg ml^{-1} polybrene and centrifuged for 2 hours at 1,000*g*, 33 °C. Cells were resuspended in fresh medium and expanded for 48 hours prior to selection. HEK293T or U2OS cells were transduced by adding viral supernatants directly to cell cultures (1:1 ratio viral supernatant to culture medium) in the presence of 8 µg ml^{-1} polybrene for 16–24 hr then replaced with fresh media.

Genome-wide CRISPR-Cas9 screens

K562 cells (ATCC) were transduced with lentiCas9-Blast (Addgene 52962) and single-cell clones were selected for stable Cas9 expression. Clonal cell lines stably expressing Cas9 were used for CRISPR-Cas9 screening. Genome-wide CRISPR-Cas9 KO screens were performed as described in refs. 67,68 with fixation and FACS staining as described in ref. 69. Briefly, sgRNA libraries cloned into pMCB320 (Addgene 101926, 101927, 101928, 101929, 101930, 101931, 101932, 101933 and 101934) targeting human protein coding genes (10 sgRNAs per gene) were packaged using third-generation lentivirus. K562 cells (250×10^6) were transduced with the genome-wide sgRNA library at a multiplicity of infection (MOI) < 1 and selected with puromycin (2 µg ml^{-1}) 48 hr after transduction. A sample of cells was analysed by FACS for mCherry expression to quantify transduction efficiency and successful sgRNA incorporation (FlowJo v10.8.1). Cells were expanded and the population was maintained 1,000-fold over the number of sgRNAs elements to maintain library representation, while passaging cells every 2 days with fresh medium. Cells in these screens were cultured without penicillin or streptomycin, and were further supplemented with uridine (50 µg ml^{-1}) and sodium pyruvate (1 mM) to maintain any mutant cells with dysfunctional mitochondria. After specified time points (days 10, 12 and 14 post-transduction), cells were pelleted, washed with PBS and fixed in ice-cold methanol (1 ml per 10 million cells) for 10 minutes at −20 °C (dropwise while vortexing) and then stained using standard intracellular FACS methods. Stained cells were sorted using a Sony SH800Z flow cytometer (~30 million cells per gate) and immediately pelleted and lysed for genomic DNA extraction. Libraries were sequenced using an Illumina NextSeq platform and sgRNA compositions between unsorted control cells and sorted cells were compared using either casTLE[68] and MAGeCK[70] software packages.

CRISPR KO clones

CRISPR-mediated mutagenesis of target genes was performed by transducing K562 cells stably expressing Cas9 (lentiCas9-Blast, Addgene 52962) with lentivirus-expressing sgRNAs (lentiGuide-Puro, Addgene 52963) targeting genes of interest. Transductions were performed as described above, and cells were selected with 2 µg ml^{-1} puromycin 48 hr after infection. Pooled mutant cells were then serially diluted to reach one cell per well in 96-well plates and clonally expanded for ~2–3 weeks. Single-cell clones were screened by PCR and western blotting to confirm homozygous disruption of genes of interest. See Supplementary Table 4 for list of sgRNA sequences.

Immunoblotting and antibodies

Protein lysates used for immunoblotting were prepared in radio immunoprecipitation assay (RIPA) buffer in the presence of protease inhibitors, unless otherwise specified. Lysates were normalized using bicinchoninic acid (BCA) assays, and standard sodium dodecyl-sulfate (SDS)-PAGE and electroblotting protocols were used. Note that samples were not boiled prior to SDS-PAGE when analysing mitochondrial-encoded proteins. The following antibodies were used in this study MT-CO1/COX1 (ABCAM, ab14705, 1:2,000), COX4I1/COX4 (CST, 4850, 1:1,000), ACTB (CST, 3700, 1:5,000), FLAG (Millipore Sigma, F1804,1:5,000), LRPPRC (Abcam, Ab97505, 1:1,000), TOMM40 (Proteintech, 18409-1-AP,1:5,000), MRPS18B (Proteintech, 16139-1-AP,1:1,000), MRPL12 (Proteintech, 14795-1-AP,1:750), WBSCR16/RCC1L (Proteintech, 13796-1-AP, 1:1,000), NDUFS1 (Abcam, ab169540,1:1,000), SDHA (Santa Cruz, sc-166947,1:10,000), UQCR4/CYC1 (Millipore Sigma, HPA001247,1:1,000), MT-ATP6 (ProteinTech, 55313-1-AP,1:1,000), ATP5H (Abcam, ab110275,1:1,000), MT-ND1 (Abcam, ab181848,1:1,000), MT-CYB (ProteinTech, 55090-1-AP,1:1,000), NME6 (Millipore Sigma, HPA017909,1:1,000), PREPL (Abcam, ab202064,1:1,000), CHCHD4 (ProteinTech 21090-1-AP,1:1,000), TRUB2 (ProteinTech,19891-1-AP, 1:1,000), RPUSD4 (Millipore Sigma HPA039689,1:1,000), TBRG4 (Sigma, HPA020582,1:1,000), GAPDH (Invitrogen, A5-15738,1:1,000), TFAM (sc-376672,1:2,000) and TACO1 (ProteinTech, 21147-1-AP, 1:1,000).

Subcellular mitochondrial and cytosolic fractionations

To obtain the cytosolic fractions, 5×10^6 K562 cells were resuspended in PBS with EDTA-free protease-inhibitor cocktail (Roche) and lysed using a 27.5 G needle. Lysates were cleared by centrifugation for 10 min at 800*g* at 4 °C. The supernatant was collected and centrifuged for 10 min at 10,000*g* at 4 °C to pellet organelles, and the supernatant was removed to obtain the cytosolic fraction. To obtain mitochondrial fractions, 30×10^6 K562 cells were pelleted and resuspended in 800 µl hypotonic buffer (10 mM Tris, pH 7.5; 10 mM NaCl; 1.5 mM $MgCl_2$) and left to swell on ice for 7.5 min. Cells were dounced in a 1 ml glass homogenizer with 20 strokes on ice. Sucrose T10E20 buffer (10 mM Tris, pH 7.6; 1 mM EDTA, pH 8.0; 2 M sucrose) was added to the lysate to bring the sucrose concentration to 250 mM and homogenized cells were centrifuged at 600*g* for 10 minutes to remove nuclei and unbroken cells. The supernatant was collected and spun at 10,000*g* to pellet mitochondria. Pellets were then washed twice with sucrose T10E20 buffer (10 mM Tris, pH 7.6; 1 mM EDTA, pH 8.0; 250 mM sucrose) before further application.

Mitochondrial IP

Mitochondrial IP was performed using K562 cells expressing an HA-mitochondrial tag (Addgene 83356) or a control MYC-mitochondrial tag (Addgene 83355) as previously described[38]. For IP, 30×10^6 cells were pelleted and washed twice in ice-cold PBS. Cells were then resuspended in 1 ml PBS with 1× EDTA-free protease inhibitor cocktail (Roche) from which 5 µl of the suspension were lysed with RIPA buffer to quantify

whole cell protein levels. The remaining suspension was lysed using eight passages through a 30 G needle. Lysates were centrifuged for 1 min at 1,000*g* to pellet unbroken cells and supernatants were incubated with 50 µl HA magnetic beads (Thermo Fisher, 88836) for 4 min. Beads were washed three times in KPBS, and then lysed in 50 µl RIPA buffer for 10 min on ice for western blotting or for use in downstream applications.

IP and mass spectrometry

We expressed C-terminal FLAG-tagged PREPL, NME6 and RCC1L for IP using the pCIG3 lentiviral vector (Addgene 78264) in K562 cells. Cells were sorted for stable expression based on GFP expression as a selectable marker. For IP of PREPL-Flag, cells were lysed in 50 mM Tris/HCl (pH 7.5), 150 mM NaCl, 1 mM $MgCl_2$, 1% NP-40, 1X EDTA-free protease inhibitor cocktail (Roche) for 20 min at 4 °C, and the lysate was cleared by centrifugation at 10,000xg for 5 min. Cleared lysates were added to washed anti-FLAG M2 beads (Sigma) and incubated with rotation at 4 °C for 16 hr. Beads were washed five times (50 mM Tris/HCl pH 7.5, 150 mM NaCl, 1 mM $MgCl_2$, 0.1% NP-40) followed by elution with 150 µg ml^{-1} 3× FLAG peptide (Sigma) at 4 °C, 1 hr. The elute was concentrated with Amicon Ultra-4 filter units with a 3 kDa MW cut-off. Bait protein enrichment was confirmed silver staining, and the remaining eluate was precipitated using a ProteoExtract protein precipitation kit (Millipore 539180) and samples were submitted to the Taplin Biological Mass Spectrometry Facility at Harvard Medical School for mass-spectrometry-based protein identification. For NME6-Flag and RCC1L-Flag, input cell numbers were increased to 50×10^6 and mitochondria were isolated prior to IP, as described above.

For co-IP analysis by western blotting, IPs were performed as above, but proteins were eluted from beads with 2× SDS-PAGE lysis buffer with boiling at 95 °C for 5 min. Supernatants were collected and analysed by SDS-PAGE and western blot analysis using indicated antibodies.

Proteinase K protection assays

Isolated mitochondria (20 µg), as described previously (1 mg ml^{-1} in 250 mM sucrose T10E20 buffer) were either left untreated or were treated for 30 min on ice with 50 µg ml^{-1} of proteinase K alone or in combination with 1% Triton X-100. To halt proteinase K treatment, 2 µl of 40 mM phenylmethanesulfonyl fluoride (PMSF) was added to all samples, and samples were incubated on ice for 20 min. Cells were then lysed in RIPA buffer with 1× EDTA-free protease inhibitor cocktail (Roche) and analysed using western blotting.

RNA abundance measurements by NanoStrings

Total RNA was purified from cells using Trizol and isopropanol precipitations. Total RNA (25–50 ng) per sample was used for each NanoStrings run. To hybridize RNA to the probe sets, first probe stocks 'A' and 'B' were diluted into working stocks by adding 4 µl of each master stock into 29 µl TE + 0.1% Tween 20. Next, 70 µl of nCounter Sprint hybridization buffer was added to a Nanostrings 24-TagSet, followed by 7 µl of the probe 'A' working stock, then 7 µl of probe 'B' working stock. In a 0.2 ml PCR tube, 8 µl of the TagSet/Probe mastermix was mixed with 25–50 ng RNA/H_20 for a 15 µl total reaction volume. Samples were hybridized in a PCR machine at 67 °C for 16 hr before loading onto a nCounter Sprint Cartridge for quantification.

qPCR detection of mtDNA levels and qRT-PCR detection of mRNA levels

DNA was isolated from cells using a Qiagen Blood and Tissue DNeasy kit. Quantitative PCR was performed using Sso EvaGreen Supermix (BioRad), adding 60 ng of template DNA per reaction and using mtDNA and nucDNA specific primers (400 nM final concentration). *MT-TRNA-LEU* (mtDNA target): Fwd = CACCCAAGAACAG GGTTTGT, Rev = TGGCCATGGGTATGTTGTTA. *B2M* (nucDNA target): Fwd = TGCTGTCTCCATGTTTGATGTATCT, Rev = TCTCTGCTCCCC ACCTCTAAGT. PCR was performed using a BioRad CFX384 Touch Real-Time PCR Detection System, with the following cycling conditions: 50 °C for 2 min, 95 °C for 10 min, 40 cycles (95 °C for 15 sec, 62 °C for 60 sec), + melt curve.

For qRT-PCR measurements of mRNA levels, 500 ng of DNAseI treated total RNA was reverse transcribed using a SuperScript III First-Strand Synthesis system. cDNA were diluted 1:100 and 1 µl was used for Taqman gene expression assays using TaqMan Fast Advanced Master Mix, no UNG (Thermo Fisher Scientific) and the following probe sets: ACTB (Hs03023880_g1), MT-CYB (Hs02596867_s1), MT-CO1 (Hs02596864_g1), and MT-RNR2 (Hs02596860_s1). Where indicated, IMT1B (MedChemExpress, cat. # HY-137067) or a DMSO vehicle control was added to cell cultures at 500 nM for the indicated amount of time before total RNA purification.

STED microscopy

STED microscopy was performed on U2OS cells transduced with lentivirus expressing Flag-tagged PREPL cDNA (pCIG3, Addgene 78264). Cells were seeded 3 days' post-transduction on coverslips (thickness 1.5H, Thor Labs CG15NH1) and fixed in 4% paraformaldehyde for 20 minutes. Standard immunocytochemistry techniques were used to stain cells with the following antibodies (anti-FLAG M2 clone 1:200; anti-TOMM40 1:200 Proteintech 18409-1-AP; anti-LRPPRC 1:200 Abcam Ab97505). Secondary antibodies: goat anti-mouse Alexa-555 (1:100); goat anti-rabbit Alexa-647(1:100). Imaging was performed at the Harvard Medical School Neurobiology Imaging Facility using the Leica SP8X STED system and deconvolution was performed post-acquisition using Hyugen's deconvolution (default parameters; Scientific Volume Imaging).

Electron microscopy

K562 cells were pelleted and fixed in 2.5% glutaraldehyde, 1.25% paraformaldehyde and 0.03% picric acid in 0.1 M sodium cacodylate buffer (pH 7.4) for 2 hr at room temperature. Samples were then processed by the HMS Electron Microscopy Facility as described: fixed cells were washed in 0.1 M cacodylate buffer and postfixed with 1% osmiumtetroxide (OsO_4)/1.5% potassium ferrocyanide ($KFeCN_6$) for 1 hr, washed twice in water, once in maleate buffer (MB) and incubated in 1% uranyl acetate in MB for 1 hr followed by two washes in water and subsequent dehydration in grades of alcohol (10 min each; 50%, 70%, 90%, 2 × 10 min 100%). The samples were then put in propyleneoxide for 1 hr and infiltrated ON in a 1:1 mixture of propyleneoxide and TAAB (TAAB Laboratories Equipment). The following day the samples were embedded in TAAB Epon and polymerized at 60 °C for 48 hr. Ultrathin sections (about 60 nm) were cut on a Reichert Ultracut-S microtome, picked up onto copper grids stained with lead citrate and examined in a JEOL 1200EX Transmission electron microscope or a $TecnaiG^2$ Spirit BioTWIN and images were recorded with an AMT 2k charge-coupled device camera.

Seahorse assays

K562 cells were seeded (75,000 cells per well) by centrifugation onto poly-L-lysine-coated 96-well Seahorse assay microplates and allowed to equilibrate in Seahorse XF RPMI Medium, pH 7.4 (Agilent, 103576-10) for 60 min, in a non-CO_2 controlled incubator before assays were performed. Respiratory parameters were measured using a Seahorse XFe96 analyser according to manufacturer's protocols with four basal measurements followed by sequential injections of oligomycin (1 µM), FCCP (2 µM) and rotenone (0.5 µM) with antimycin A (0.5 µM), where three measurements were taken after each injection. To measure the activity for specific OXPHOS complexes, the experiments were performed in permeabilized K562 cells, as described in ref. 71. Briefly, 30,000 K562 cells were seeded on poly-L-lysine-coated 96-well plate and just prior to measurements, medium was replaced by MAS-BSA buffer (70 mM sucrose, 220 mM mannitol, 10 mM KH_2PO_4, 5 mM $MgCl_2$, 2 mM Hepes (pH 7.2), 1 mM EGTA and 4 µg ml^{-1} BSA). Three basal

measurements were taken, upon which the cells were permeabilized using XF Plasma Membrane Permeabilizer (1.5 nM final concentration; Agilent) together with 1 mM ADP and the following specific respiratory complex substrates: Complex I = pyruvate/malate (5 mM/2.5 mM); Complex IV = *N*,*N*,*N*,*N*-tetramethyl-*p*-phenylenediamine/ascorbate (0.5 mM in 2 mM final concentration). These were followed by injections with oligomycin (1 µg ml^{-1} final) and respective complex inhibitors (Complex I, 1 µM rotenone; Complex IV, 20 mM sodium azide).

Complex IV enzymatic activity assays

Mitochondria were isolated from cells as described above using hypotonic lysis and differential centrifugation. Proteins were extracted from isolated mitochondria in the presence of protease inhibitors (Halt Protease Inhibitor Cocktail, Thermo Fisher) and protein content was quantified using BCA assays. Complex IV enzyme activity was measured colorimetrically in antibody-coated microplates by measuring the oxidation of cytochrome c according to the manufacturer's instructions (Abcam ab109909).

Pseudouridine sequencing

CMC (*N*-cyclohexyl-*N*′-(2-morpholinoethyl)carbodiimide metho-*p*-toluene sulfonate; Santa Cruz Biotechnology)-based detection of pseudouridine RNA modifications was performed as described previously[43,72]. Briefly, mitochondria were fractionated from cells as described above and RNA was purified using standard Trizol and isopropanol precipitation methods. RNA (3 µg) from each sample was split into −CMC and +CMC conditions (2 µg used for +CMC and 1 µg used for −CMC) and adjusted to 20 µl each with water. RNA was denatured by adding 2.9 µl of 20 mM EDTA pH 8.0, heated for 3 min at 80 °C, then returned to ice. CMC (0.5 M) was prepared fresh in BEU buffer (50 mM bicine, pH 8.5, 4 mM EDTA, 7 M urea) just before use, and 100 µl of either CMC or BEU buffer was added to −CMC or +CMC samples, respectively, and incubated at 40 °C for 45 min mixing at 1,000 rpm in a thermomixer. RNA was precipitated (sodium acetate, 100% ethanol, glycoblue) and then CMC bound to U/G residues was reversed by heating RNA samples at 50 °C for 2 hr with mixing at 1,000 rpm in sodium carbonate buffer (pH 10.4, 50 mM Na_2CO_3, 2 mM EDTA). RNA was precipitated (sodium acetate, 100% ethanol, glycoblue), washed and resuspended in 15 µl of water. RNA was quantified using a Nanodrop, and RNA-sequencing libraries were made using the SMARTer Stranded Total RNA Sample Prep Kit - HI Mammalian (Takara). Libraries were sequenced at the Bauer Core Facility (Harvard University) using 150 bp paired-end reads using an Illumina NovaSeq. Pseudouridine levels were quantified as described previously[43]. Briefly, reads were aligned to the genome and variants at each position were detected using Samtools mpileup. As CMC-bound pseudouridine bases cause deletions during reverse transcription, we determined the number of deletions at each base across the mitochondrial genome normalized to total read counts (corrected for deletions in −CMC conditions) using previously published software written for this purpose[43].

^{35}S metabolic labelling

K562 cells were grown at 5×10^5 cells ml^{-1} in FBS-supplemented RPMI media. For ^{35}S metabolic labelling, 3×10^6 cells were washed once with PBS and resuspended in labelling media (RPMI without cystine, methionine and cysteine, MP Biomedical 1646454, supplemented with dialysed FBS and glutamine). Cells were equilibrated for 30 min at 37 °C and 5% CO_2 and then treated with 100 µg ml^{-1} of anisomycin for 10 min 200 µCi ml^{-1} of EasyTag labelling mix (^{35}S-cysteine/^{35}S-methionine, PerkinElmer NEG772007MC) was added for 30 min or 60 min. Subsequently, cells were washed twice with ice-cold PBS and lysed in RIPA buffer with EDTA-free protease inhibitor cocktail (Roche). Lysates were then separated on a 17.5% acrylamide gel for 6 hr at 150 V and transferred onto a 0.22 µM nitrocellulose membrane using semi-dry transfer methods and signals were imaged using autoradiography.

4sU metabolic labelling

Incorporation of 4sU into K562 cells was determined by measuring the fractions of unlabelled mtRNA by NanoStrings after 4sU labelling and depletion, as described in ref. 73. In short, K562 cells were labelled with 500 µM 4sU for 30 min and lysed in Trizol. RNA was purified using isopropanol precipitations with the addition of spike-ins using in vitro transcribed RNA: ERCC-000148, as an unlabelled control. RNA was denatured at 60 °C for 10 min and biotinylated using 5 µg ml^{-1} biotin-MTS (Biotium) in 20% dimethylformamide (Sigma), 20 mM Hepes pH 7.4 and 1 mM EDTA with incubation for 30 min. Free biotin was removed using phase-lock heavy gel tubes (5prime), and then the mixture of unlabelled RNA and biotinylated RNA was incubated with streptavidin beads (uMACS Streptavidin kits, Miltenyi Biotec) following the manufacturer's protocol. After incubation, RNA levels were quantified and equal amounts of RNA–bead mixture (3 µg RNA; 100 µl beads) were loaded on a uMACS column and washed with 100 mM Tris pH 7.5, 10 mM EDTA, 1 M NaCl, 0.1% Tween 20 to collect unlabelled RNA in the flow-through. Collected RNA was purified using miRNeasy kits (Qiagen) with DNAse treatments (Qiagen). MitoStrings measurements were performed as described previously.

Blue native PAGE

BN-PAGE was adapted from previously published protocols[74]. In short, 50 µg of isolated mitochondria, as described above, was resuspended in 20 µl sample buffer cocktail (5 µl 4X NativePAGE sample buffer, 8 µl of 5% digitonin and 7 µl of water). The suspension was left on ice to solubilize for 20 min, after which the lysate was cleared with centrifugation at 20,000*g* for 10 min at 4 °C. Coomassie G-250 (2 µl) was added to the supernatant and proteins were separated using NativePAGE 3–12% gradient gels (Thermo Fisher Scientific). During electrophoresis, inner chambers were filled with dark blue cathode buffer (Bis-tris 50 mM, Tricine 50 mM and 0.02% Coomassie blue G-250) and outside chambers were filled with running buffer (Bis-tris 50 mM). Gels were run for 30 min at 150 V, upon which the dark blue running buffer was replaced with light blue running buffer (Bis-tris 50 mM, Tricine 50 mM and 0.001% Coomassie blue G-250) and run for an additional 90 min at 250 V. Proteins were transferred onto PVDF membranes using wet transfer methods at 200 mA for 90 min, fixed with 8% acetic acid, rinsed twice with water, and then air dried. Dried membranes were then activated in 100% methanol for 5 min, followed by methanol and water rinses to remove coomassie staining, and then blocked using 5% skim milk in TBST. OXPHOS complexes were analysed by immunoblotting with indicated antibodies towards each complex.

Recombinant NME6–RCC1L expression and in vitro NDPK assays

Recombinant RCC1L (amino acids 32–464) was expressed recombinantly as described previously[75] by cloning corresponding cDNA into pGEX-4T-1 with an N-terminal GST tag. For recombinant NME6-WT and NME6-H137A, cDNA corresponding to the full-length NME6 CDS was cloned into pET30a with an N-terminal 6xHis tag. Constructs were transformed into T7 Express lysY/Iq *E. coli* cells (NEB, C3013I) and grown at 37 °C with shaking until cultures reached OD_{600} = 0.6–0.8. Protein expression was induced by the addition of IPTG (1 mM IPTG, 4 hr, 37 °C for RCC1L or 0.1 mM IPTG, overnight, 18 °C for NME6). Bacteria were pelleted and lysed by sonication in lysis buffer (30 mM Tris-HCl pH 8, 0.5 M NaCl, 7 mM 2-mercaptoethanol, 1× Complete EDTA-free Protease Inhibitor Cocktail) and the resulting lysates were clarified by centrifugation. Cleared lysates were then purified using glutathione agarose in the case of GST-RCC1L or Ni-NTA agarose (Qiagen) in the cases of NME6. Proteins were eluted off beads and dialysed overnight into SEC buffer for NME6 (25 mM Hepes pH 7.5, 300 mM NaCl, and 5 mM DTT) or dialysis buffer for RCC1L (10 mM Tris-HCl pH 8, 0.25 M NaCl, 2 mM 2-mercaptoethanol). NME6-WT and NME6-H137A were further purified by size-exclusion chromatography (HiLoad 16/60 S200 column, Cytiva 28989335), and fractions were pooled, concentrated and

analysed for purity by SDS-PAGE. All proteins were stored at −80 °C with the addition of 10% glycerol.

ATP hydrolysis reactions were performed by incubating the indicated protein amounts in the following reaction buffer (20 mM Tris pH 7.5, 100 mM NaCl, 10 mM $MgCl_2$, 1 mM DTT, and 500 µM ATP) for 30 min at 37 °C. Released free orthophosphate was quantified using the Malachite Green Phosphate Assay kit (Millipore Sigma). Samples with ATP containing reaction buffer lacking proteins and proteins alone lacking ATP were used to correct for any background readings. NDPK phosphorylation was performed by pre-binding 15 µg of GST-RCC1L to glutathione agarose beads for 30 min at room temperature with rotation followed by the addition of 20 µg NME6-WT or H137A in reaction buffer (50 mM Tris pH 7.5, 150 mM NaCl, and 10 mM $MgCl_2$). Bound complexes were allowed to form for 2 hr at 4 °C with rotation, and subsequently unbound proteins were washed from the beads. Washed NME6–RCC1L-bound beads were resuspended in reaction buffer supplemented with 10 µM cold ATP and 4 µCi of gamma-^{32}P ATP (PerkinElmer, BLU002250UC). Reactions were incubated for 30 min at 30 °C and, subsequently, beads were washed five times to remove free ATP. Reactions were split in half, with one half used to determine protein phosphorylation and the other half used for phosphate transfer reactions. To determine protein phosphorylation, proteins were eluted from beads with SDS-sample buffer (15 min at room temperature, no boiling) and then analysed by SDS-PAGE and autoradiography. To determine phosphate transfer activity, washed beads were resuspended with cold acceptor nucleotides (1 mM UDP or CDP in reaction buffer) and incubated for 30 min at 30 °C. UTP or CTP formation was analysed by autoradiography using TLC on PEI-cellulose plates (Millipore Sigma 1.05579) using 1.2 M LiCl as a solvent.

Sucrose gradient fractionations

50×10^6 cells K562 cells were grown at 5×10^5 cells ml^{-1} for sucrose gradient fractionations. Upon removing medium, cells were rinsed with ice-cold PBS and resuspended in 600 µl of mitoribosome lysis buffer (0.25% lauryl maltoside, 50 mM NH_4Cl, 20 mM $MgCl_2$, 0.5 mM DTT, 10 mM Tris, pH 7.5, and 1× EDTA-free protease inhibitor cocktail (Roche)). Lysates were clarified by centrifugation at 10,000*g* for 5 min. To isolate mitoribosomes, 450 µl of clarified lysate was layered on top of 12 ml 10–50% linear sucrose gradients and centrifuged at 40,000 rpm (273,620*g*) for 3 h at 4 °C using an SW41Ti rotor. Gradients were fractionated into 800 µl fractions using a BioComp instrument and mitoribosomes were followed with western blotting using antibodies against small (MRPS18B) and large (MRPL12) mitoribosome subunits.

Nanopore direct RNA sequencing

Total RNA was extracted using Trizol and isopropanol precipitation, followed by polyA+ enrichment of mRNAs using a Dynabeads mRNA Purification Kit (Thermo Fisher, 61006). PolyA+ (500 ng) RNA was used for input into the Oxford Nanopore Technologies Direct RNA-sequencing library preparation kit (SQK-RNA002). Steps were performed following the manufacturer's protocol except for the following changes: (1) RNA CS was not added to the initial ligation mix and instead replaced with nuclease-free water and (2) ligation of the RT adapter was extended from 10 to 15 minutes. The resulting libraries were sequenced on a MinION device (Oxford Nanopore Technologies) for up to 72 hours. Sequencing reads were basecalled live with MinKNOW (release 20.10.3 or later) and filtered for basecalling threshold >7. U bases were substituted for T bases in the resulting reads, followed by alignment to the reference hg38 genome using minimap2 (ref. 76) with parameters -ax splice -uf -k14. Multi-mapping reads were included in downstream analyses. 5′-end processing status of each read mapping to mt-mRNAs was determined by mapping the location of the 5′-end of the read relative to the start of the transcript (−15 to +50 nt from transcript start). Reads that started in the transcript start window of a gene were classified as 'processed' and reads that started upstream of this window were classified as 'unprocessed'. Poly(A) tail lengths were measured using nanopolish[77]. Reads with qc_tag 'PASS' and with the 3′-end mapping within −15 to +15 nt of the transcript end were included in poly(A) tail length analyses.

In organello mitochondrial transcription assays

Mitochondria were purified by subcellular fractionation or rapid mitochondrial IP as described above. Transcription assays were performed as described in ref. 78. Briefly, purified mitochondria were labelled with 30 µCi of alpha-^{32}P UTP (PerkinElmer BLU007H250UC) in transcription buffer (10 mM Tris pH 7.5, 25 mM sucrose, 75 mM sorbitol, 100 mM KCl, 10 mM K_2HPO_4, 50 µM EDTA, 5 mM MgCl2, 10 mM glutamate, 2.5 mM malate, 1 mg ml^{-1} BSA, 1 mM ADP) at 37 °C for 20 min. then chased with cold UTP in transcription buffer for 5 min. at 37 °C. Mitochondria were washed three times with wash buffer (10 mM Tris pH 6.8, 0.15 mM $MgCl_2$, 10% glycerol) followed by RNA extraction using Trizol and isopropanol precipitation. RNA was resuspended in 2× urea sample buffer (Thermo Fisher) and separated by denaturing PAGE using Novex 6% TBE-urea gels (Thermo Fisher). Newly transcribed RNAs containing ^{32}P UTP were visualized by autoradiography.

Mitochondria IP for metabolomics

Mitochondrial IP followed by mass spectrometry was adapted from ref. 38. Briefly, mitochondria were immunoprecipitated from 50×10^6 K562 cells as described above. Pelleted cells were washed twice with ice-cold KPBS, followed by homogenization using 25 strokes with a polytetrafluoroethylene (PTFE) dounce homogenizer (VWR) and centrifuged for 2 min at 1,000*g*, 4 °C. The supernatant was resuspended with 200 µl anti-HA magnetic beads and the mixture was incubated at 4 °C using an end-over-end rotator for 3.5 min. Beads were washed three times in ice-cold KPBS, and were immediately resuspended in either protein extraction or metabolite extraction buffer.

Metabolite profiling by mass spectrometry for detection of polar metabolites

For whole cell measurements, 1×10^6 K562 cells were washed with ice-cold 0.9% NaCl briefly and metabolites were extracted using 200 µl buffer (80% methanol, 25 mM ammonium acetate and 2.5 mM Na-ascorbate prepared in LC-MS water, supplemented with isotopically labelled amino acid standards (Cambridge Isotope Laboratories, MSK-A2-1.2), aminopterin, and reduced glutathione standard (Cambridge Isotope Laboratories, CNLM-6245-10)) for 10 min. The samples were vortexed for 10 sec, then centrifuged for 10 min at 21,000*g* to pellet cell debris. The supernatant was dried on ice using a liquid nitrogen dryer. Metabolites were reconstituted in 20 µl water supplemented with QReSS (Cambridge Isotope Laboratories, MSK-QRESS-KIT) and 1 µl was injected into a ZIC-pHILIC 150 × 2.1 mm (5 µm particle size) column (EMD Millipore) operated on a Vanquish Flex UHPLC Systems (Thermo Fisher Scientific). Chromatographic separation was achieved using the following conditions: buffer A was acetonitrile; buffer B was 20 mM ammonium carbonate, 0.1% ammonium hydroxide in water. Gradient conditions were: linear gradient from 20% to 80% B; 20–20.5 min: from 80% to 20% B; 20.5–28 min: hold at 20% B at 150 mL/min flow rate. The column oven and autosampler tray were held at 25 °C and 4 °C, respectively. MS data acquisition was performed using a QExactive benchtop orbitrap mass spectrometer equipped with an Ion Max source and a HESI II probe (Thermo Fisher Scientific, San Jose, CA, USA) and was performed in positive and negative ionization mode in a range of m/z = 70–1,000, with the resolution set at 70,000, an AGC target of 1×10^6, and the maximum injection time (Max IT) at 20 msec. HESI settings were: sheath gas flow rate: 35; aux gas flow rate: 8; sweep gas flow rate: 1; spray voltage 3.5 (pos); 2.8 (neg); capillary temperature: 300 °C; S-lens RF level: 60; aux gas heater temp: 350 °C. An independent injection was performed for more specific detection of nucleotides. Mass spectrometer was operated in full scan mode in

a range of m/z = 200–700 and m/z = 300–600 in negative and positive ionization mode respectively, with the resolution set at 70,000, the AGC target at 1×10^6, and the maximum injection time (Max IT) at 40 msec. HESI settings were: sheath gas flow rate: 35; aux gas flow rate: 8; sweep gas flow rate: 1; spray voltage 3.5 (pos); 2.8 (neg); capillary temperature: 400 °C; S-lens RF level: 60; aux gas heater temp: 450 °C.

Data analysis for metabolite profiling

Relative quantification of polar metabolites was performed with TraceFinder 5.1 (Thermo Fisher Scientific) using a 7 ppm mass tolerance and referencing an in-house library of chemical standards. Pooled samples and fractional dilutions were prepared as quality controls and injected at the beginning and end of each run. In addition, pooled samples were interspersed throughout the run to control for technical drift in signal quality as well as to serve to assess the coefficient of variability (CV) for each metabolite. Data from TraceFinder were further consolidated and normalized with an in-house R script: (https://github.com/FrozenGas/KanarekLabTraceFinderRScripts/blob/main/MS_data_script_v2.4_20221018.R). Briefly, this script performs normalization and quality control steps: (1) extracts and combines the peak areas from TraceFinder output.csvs; (2) calculates and normalizes to an averaged factor from all mean-centred chromatographic peak areas of isotopically labelled amino acids internal standards within each sample; (3) filters out low-quality metabolites based on user inputted cut-offs calculated from pool reinjections and pool dilutions; (4) calculates and normalizes for biological material amounts based on the total integrated peak area values of high-confidence metabolites. In this study, the linear correlation between the dilution factor and the peak area cut-offs are set to RSQ > 0.95 and the CV < 30%. Finally, data were log transformed and Pareto scaled within the MetaboAnalyst-based statistical analysis platform[79] to generate PCA, PLSDA and heatmaps. For mt-IP metabolomics, samples were normalized to total protein in purified mitochondria determined using BCA assays.

Data analysis for ^{13}C-glucose isotope tracing

K562 cells were glucose-deprived in glucose-free RPMI-1640 media for 2 hr. followed by metabolic labelling in glucose-free RPMI-1640 supplemented with either 10 mM ^{13}C-glucose (Cambridge Isotope Laboratories) or 10 mM standard glucose (Sigma). mt-IP was performed as described above, after 22 hr of growth in labelling media. Analysis for ^{13}C-glucose tracing experiments was performed on Compound-Discoverer (CD) 3.3 (Thermo Fisher Scientific) and TraceFinder (TF) 5.1. For CD, an in-house database was used to first filter out features and only consider compounds at level 1 of identification certainty[80]. Additional background filtering and sample normalization steps as well as normalization for natural isotope abundance of reported compound labelling efficiency were performed within the software. Briefly, cut-offs and biological factor normalizations were calculated from pool reinjection samples. Compounds which were fivefold above background levels were only considered in further analysis. For TF analysis individual isotopologues were quantified using a 7 ppm mass tolerance and referencing an in-house library of chemical standards.

Mitoribosome profiling

50×10^6 cells K562 cells were grown in RPMI at 5×10^5 cells ml^{-1} for mitoribosome profiling. Culture medium was removed, and the cells were rinsed with ice-cold PBS and resuspended in 600 µl of mitoribosome lysis buffer (0.25% lauryl maltoside, 10 mM Tris pH 7.5, 50 mM NH_4Cl, 20 mM $MgCl_2$, 0.5 mM DTT, and 1× EDTA-free protease inhibitor cocktail (Roche)) and homogenized briefly with a dounce homogenizer. Lysates were digested using 8 units per µl of RNaseI (LGC) for 30 min. at room temperature to generate mitoribosome footprints followed by the addition of 80 units SUPERaseIn (Thermo Fisher Scientific) and a 5 min spin at 10,000g to clarify the lysate. The mitoribosomes were isolated by loading 450 µl of clarified lysate onto 12 ml 10–50% linear sucrose gradients and centrifugation at 40,000 rpm for 3 h at 4 °C using an SW41Ti rotor. Gradients were fractionated into 800 µl fractions using a BioComp instrument and mitoribosomes were detected using western blots using antibodies against MRPL12 and MRPS18B. From the mitomonosome fraction, RNA was extracted using 1:1 acid phenol/chloroform extraction and separated on 15% polyacrylamide TBE-urea gel to collect RNA fragments between 28–40 nucleotide size. Libraries were prepared as previously described along with the modification for mitoribosome library preparations[11]. Samples were sequenced using an Illumina NextSeq 500 (single-end reads, 75 cycles) and analysed using the following pipeline (https://github.com/churchmanlab/human-mitoribosome-profiling). Briefly, reads were trimmed and aligned using STAR, periodicity and A-site transformations were determined, and synthesis rates in transcripts per million (TPM) were calculated for mtRNAs by counting reads on genes using featureCounts (Subread). Translational efficiency was calculated by dividing the TPMs of ribosome footprints by the TPMs for total RNA sequencing for each mtRNA.

Statistics and reproducibility

All statistical testing was performed using either R or GraphPad Prism software. No statistical methods were used to predetermine sample sizes. No data were excluded from the analyses. These experiments were not randomized. Data collection and analysis were not performed blind to the conditions of the experiments. Data met the assumptions of statistical tests indicated.

Reporting summary

Further information on research design is available in the Nature Portfolio Reporting Summary linked to this article.

Data availability

Deep-sequencing data that support the findings of this study have been deposited in the Gene Expression Omnibus under accession code GSE224819. Mass spectrometry data have been deposited with ProteomeXchange with the primary accession code PXD044812. Metabolomics data are available in Supplementary Table 3. Source data are provided with this paper. All other data supporting the findings of this study are available from the corresponding author on reasonable request.

Code availability

Data from TraceFinder was consolidated and normalized with an in-house R script: https://github.com/FrozenGas/KanarekLabTraceFinderRScripts/blob/main/MS_data_script_v2.4_20221018.R. Mitoribosome profiling analysis was done using the Churchman lab's pipeline: https://github.com/churchmanlab/human-mitoribosome-profiling.

References

67. Kramer, N. J. et al. CRISPR–Cas9 screens in human cells and primary neurons identify modifiers of C9ORF72 dipeptide-repeat-protein toxicity. *Nat. Genet.* **50**, 603–612 (2018).
68. Morgens, D. W., Deans, R. M., Li, A. & Bassik, M. C. Systematic comparison of CRISPR/Cas9 and RNAi screens for essential genes. *Nat. Biotechnol.* **34**, 634–636 (2016).
69. Kim, G. et al. Genome-wide CRISPR screen reveals v-ATPase as a drug target to lower levels of ALS protein ataxin-2. *Cell Rep.* **41**, 111508 (2022).
70. Li, W. et al. MAGeCK enables robust identification of essential genes from genome-scale CRISPR/Cas9 knockout screens. *Genome Biol.* **15**, 554 (2014).
71. Salabei, J. K., Gibb, A. A. & Hill, B. G. Comprehensive measurement of respiratory activity in permeabilized cells using extracellular flux analysis. *Nat. Protoc.* **9**, 421–438 (2014).

72. Carlile, T. M., Rojas-Duran, M. F. & Gilbert, W. V. in *Methods in Enzymology* (ed. He, C.) Vol. 560, Ch. 11, 219–245 (Academic, 2015).
73. Smalec, B. M. et al. Genome-wide quantification of RNA flow across subcellular compartments reveals determinants of the mammalian transcript life cycle. Preprint at *bioRxiv* https://doi.org/10.1101/2022.08.21.504696 (2022).
74. Jha, P., Wang, X. & Auwerx, J. Analysis of mitochondrial respiratory chain supercomplexes using blue native polyacrylamide gel electrophoresis (BN-PAGE). *Curr. Protoc. Mouse Biol.* **6**, 1–14 (2016).
75. Koyama, M., Sasaki, T., Sasaki, N. & Matsuura, Y. Crystal structure of human WBSCR16, an RCC1-like protein in mitochondria. *Protein Sci.* **26**, 1870–1877 (2017).
76. Li, H. Minimap2: pairwise alignment for nucleotide sequences. *Bioinformatics* **34**, 3094–3100 (2018).
77. Workman, R. E. et al. Nanopore native RNA sequencing of a human poly(A) transcriptome. *Nat. Methods* **16**, 1297–1305 (2019).
78. Jiang, S. et al. TEFM regulates both transcription elongation and RNA processing in mitochondria. *EMBO Rep.* **20**, e48101 (2019).
79. Xia, J., Sinelnikov, I. V., Han, B. & Wishart, D. S. MetaboAnalyst 3.0–making metabolomics more meaningful. *Nucleic Acids Res.* **43**, W251–W257 (2015).
80. Salek, R. M., Steinbeck, C., Viant, M. R., Goodacre, R. & Dunn, W. B. The role of reporting standards for metabolite annotation and identification in metabolomic studies. *Gigascience* **2**, 13 (2013).

Acknowledgements

We would like to thank C. Guegler for critical reading of the manuscript, S. Adamson for advice on BN-PAGE experiments, P. Kranzusch for advice on TLC assays, and J. Warner for help with fast protein liquid chromatography protein purification. This research was conducted with support from the HMS Electron Microscopy Facility, the HMS Taplin Mass Spectrometry Facility, the HMS MicRoN and Neurobiology Imaging facilities, the Bauer Core facility of Harvard University and the Boston Children's Hospital Molecular Genetics Core. This work was supported by the National Institutes of Health (R01-GM123002 to L.S.C., F32-GM139244 to N.J.K.) and the Ludwig Neurodegenerative Disease Seed Grants Program at Harvard Medical School. K.C. is supported by post-doctoral fellowships from the Fonds de Recherche du Québec - Santé and the Canadian Institutes of Health Research. B.P. and N.K. are supported by the Smith Family Foundation. N.K. is a Pew Scholar.

Author contributions

Conceptualization was performed by N.J.K. and L.S.C. Experimental investigation was performed by N.J.K., G.P., R.S.I. and I.S. Software/formal analysis was performed by N.J.K, G.P., K.C. and H.E.M. Metabolite profiling was performed by B.P. and N.K. The Article was written by N.J.K., G.P., and L.S.C. All authors reviewed and edited the Article.

Competing interests

The authors declare no competing interests.

Additional information

Extended data is available for this paper at https://doi.org/10.1038/s41556-023-01244-3.

Supplementary information The online version contains supplementary material available at https://doi.org/10.1038/s41556-023-01244-3.

Correspondence and requests for materials should be addressed to L. Stirling Churchman.

Peer review information *Nature Cell Biology* thanks the anonymous reviewers for their contribution to the peer review of this work.

https://doi.org/10.1038/s41556-023-01244-3

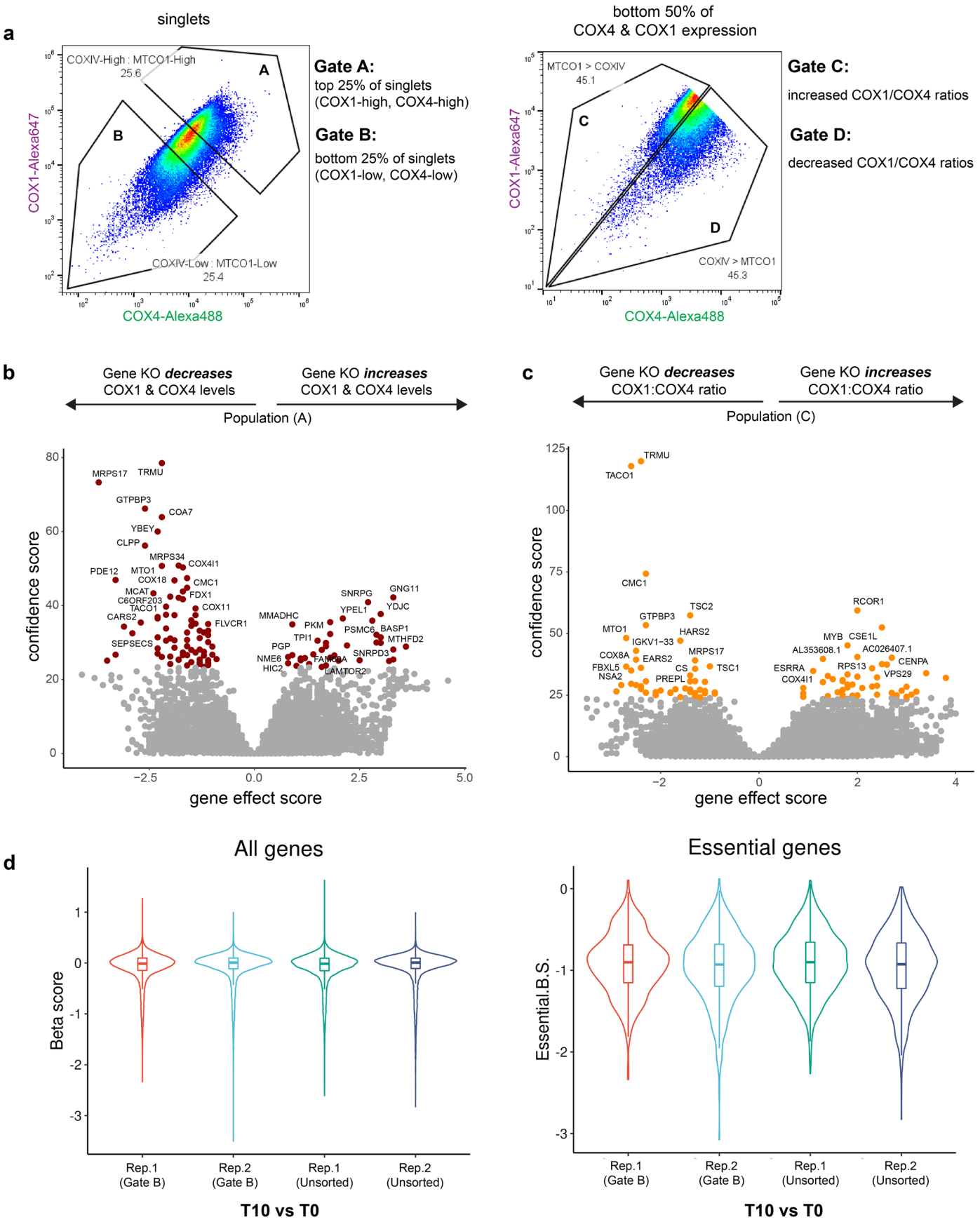

Extended Data Fig. 1 | See next page for caption.

https://doi.org/10.1038/s41556-023-01244-3

Extended Data Fig. 1 | (**a**) Gating strategies used during flow cytometry depicting populations sorted for analysis in CRISPR screens. (**b, c**) Volcano plots of gene effect score (enrichment or depletion of sgRNAs in the sorted population relative to unsorted controls) vs confidence scores of genes identified in Population A and Population C. Coloured points = genes passing a 10% FDR threshold. (**d**) Quality control metrics for CRISPR screens showing violin plots of the beta scores (degree of selection, negative values = negative selection, positive values = positive selection; MAGeCK) for all genes (left; n = 20,467 genes) or known essential genes (right) for each sample after 10 days in culture (T10) relative to screen day 0 (T0). sgRNAs targeting known essential genes were negatively selected over time indicating functional Cas9 activity and consistent sgRNA library behaviour (n = 625 genes). Box plots: centre line, median; box limits, upper and lower quartiles; whiskers, 1.5 × interquartile range. Source numerical data and unprocessed blots are available in source data.

https://doi.org/10.1038/s41556-023-01244-3

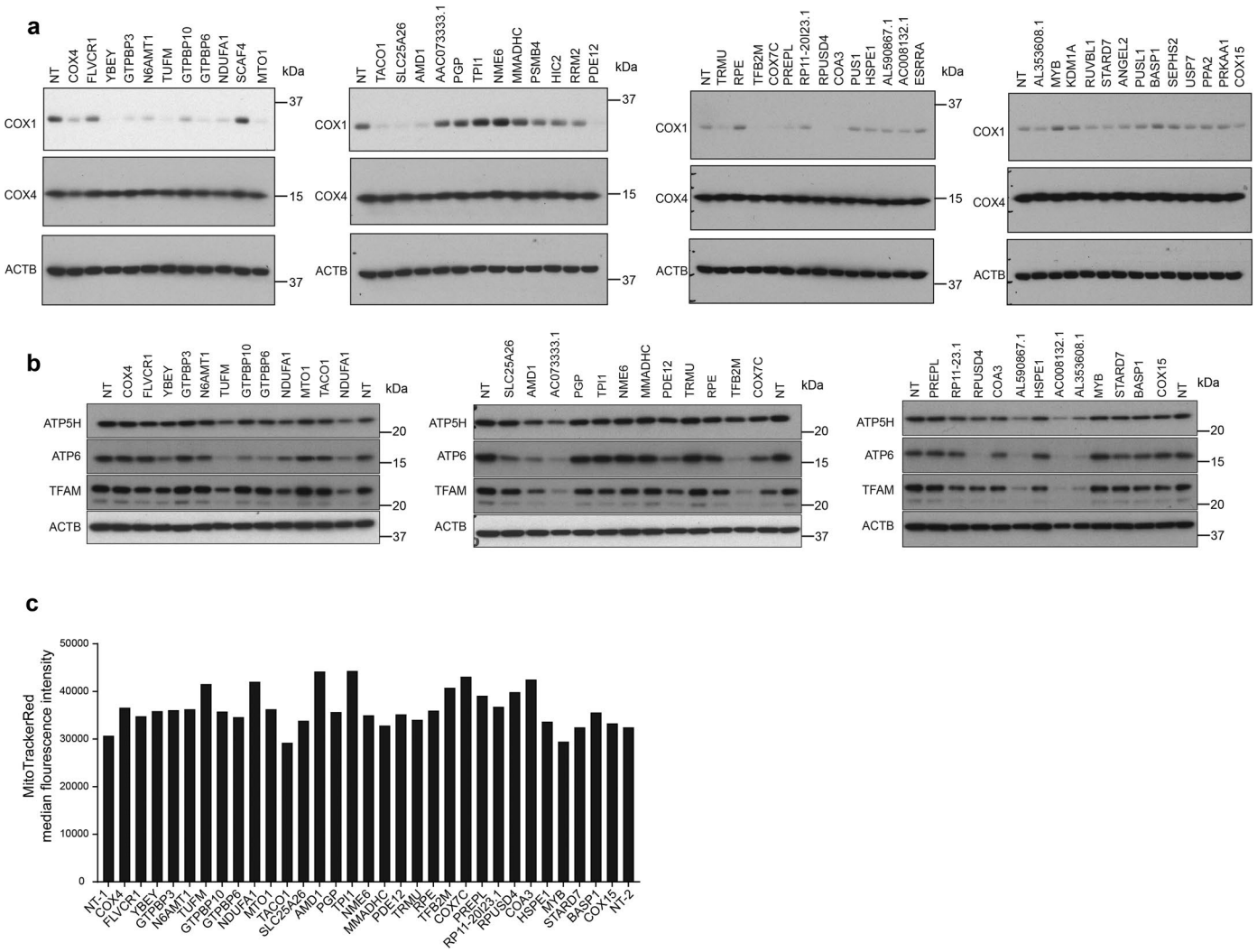

Extended Data Fig. 2 | (**a**) Western blot validation of screen hits after individual sgRNA transductions (NT sgRNA). Representative blots from 2 independent experiments. (**b**) TFAM and Complex V subunit levels (mito-encoded ATP6, nuclear-encoded ATP5H) levels in selected hits measured by western blotting. Representative blots from 2 independent experiments. (**c**) FACS analysis of live cells transduced with individual sgRNAs and stained with MitoTrackerRed CMXros (data are median fluorescence intensities from 20,000 analysed cells). Source numerical data and unprocessed blots are available in source data.

https://doi.org/10.1038/s41556-023-01244-3

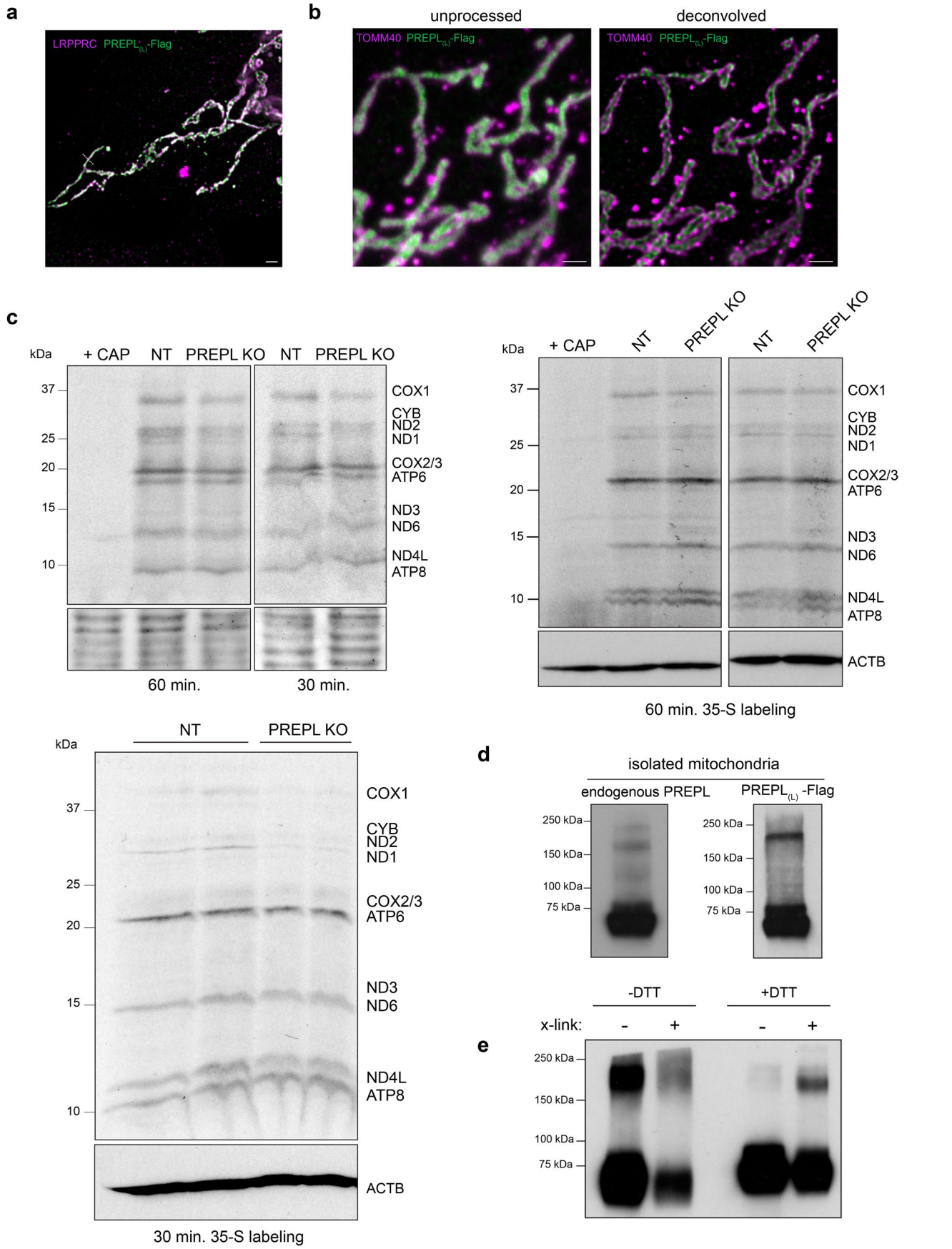

Extended Data Fig. 3 | See next page for caption.

https://doi.org/10.1038/s41556-023-01244-3

Extended Data Fig. 3 | (**a**) Representative STED micrograph of LRPPRC (magenta; matrix marker) and $PREPL_{(L)}$-Flag (green) co-staining. Quantification of line scans (across indicated dashed line) of pixel intensity for each fluorescence channel appear in Fig. 3d. Experiment repeated twice. (**b**) STED micrograph showing raw signal compared to deconvolved images using Hyugen's deconvolution (default parameters, Scientific Volume Imaging; scale bars = 500 nm). Experiment repeated twice. (**c**) 35S-methionine gels to analyse newly synthesized mitochondrial translation products (replicate gels used in quantification presented in Fig. 4f). (**d**) Immunoblot analysis of PREPL high molecular weight species (potential dimer from purified mitochondrial lysates (K562 endogenous PREPL, left; K562 cells expressing PREPL-Flag, right). Representative blots from 3 independent experiments. (**e**) Immunoblot analysis of PREPL putative dimerization after PREPL-Flag IP with or without cross-linking (x-link = crosslinked with 1 mM DSP (dithiobis(succinimidyl propionate, 2 hr. at 4 C and quenched with Tris pH 7.5) and then treated −/+ reducing agent DTT (50 mM, 95 C for 10 min) after IP. Representative blots from 2 independent experiments. Unprocessed blots are available in source data.

https://doi.org/10.1038/s41556-023-01244-3

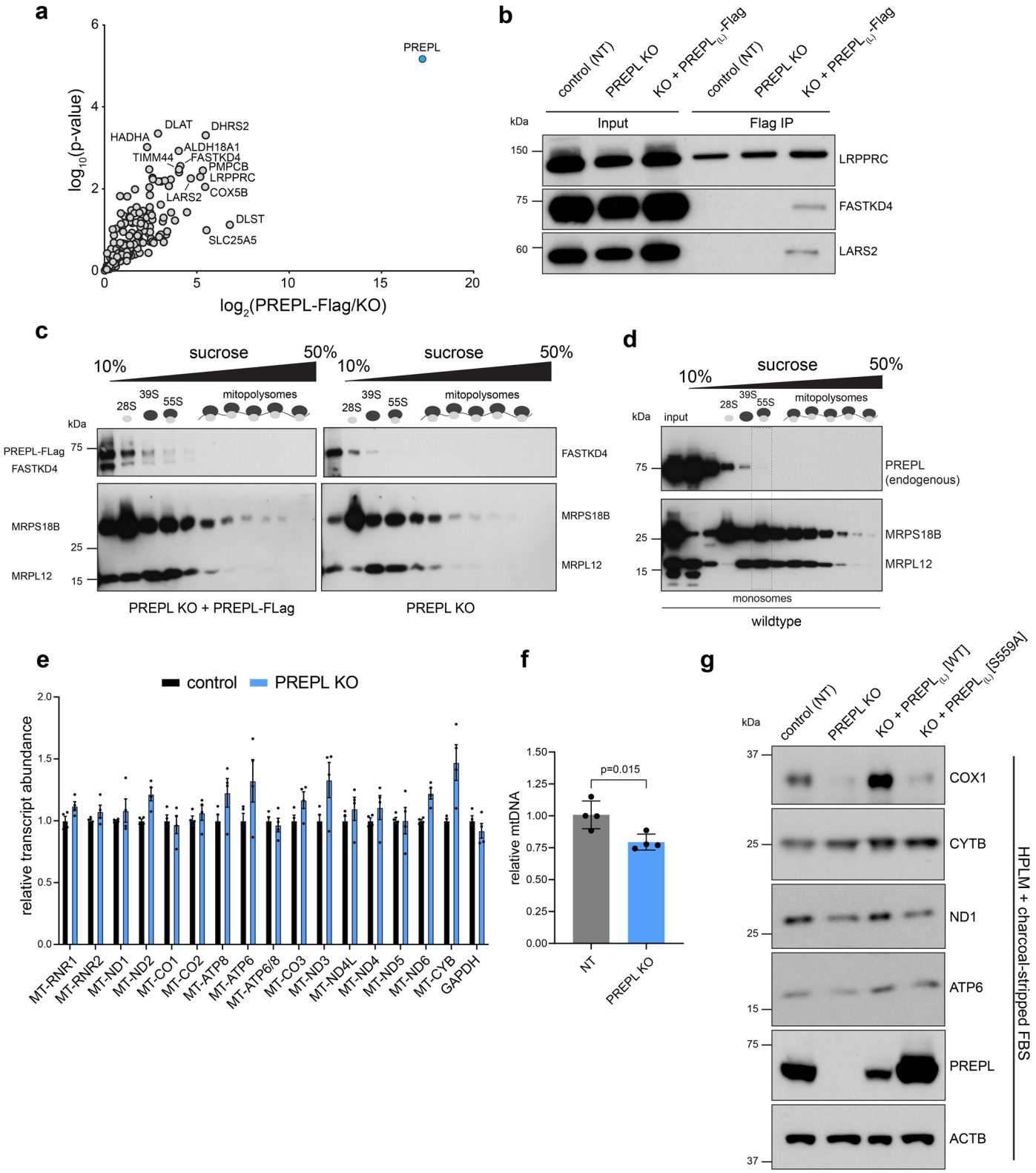

Extended Data Fig. 4 | (**a**) Mass spectrometry identification of proteins in anti-Flag IPs from PREPL KO or PREPL KO + $PREPL_{(L)}$-Flag whole cell lysates ($PREPL_{(L)}$-Flag = bait in blue; n = 3 replicates, two-tailed Welch's t-test). (**b**) Co-IP (PREPL-Flag = bait) and western blot analysis of selected mass spectrometry-identified proteins, FASTKD4/TBRG4 and LARS2. Experiment repeated twice. (**c, d**) Sucrose gradient centrifugation and fractionation with western blot detection of mitoribosome subunits, as well as (**c**) $PREPL_{(L)}$-Flag and FASTKD4 (MRPS18B = small mitoribosome subunit, MRPL12 = large mitoribosome subunits), and (**d**) endogenous PREPL. Experiment repeated twice. (**e**) MitoStrings measurements of mtRNA abundance in control and PREPL KO cells (n = 4 replicates from 2 independent experiments, data are means −/+ SEM). (**f**) qPCR measurements of mtDNA levels normalized to nuclear DNA content (mito target = *MT-TL1*, nuclear target = *B2M*; n = 4 replicates from 2 independent experiments, two-tailed t-test, data are means +/− SD). (**g**) Western blot analysis of OXPHOS subunits in NT, PREPL KO, KO + PREPL-WT, and KO + PREPL-S559A, in HPLM media supplemented with charcoal-stripped FBS. Representative blots from 2 independent experiments. Source numerical data and unprocessed blots are available in source data.

https://doi.org/10.1038/s41556-023-01244-3

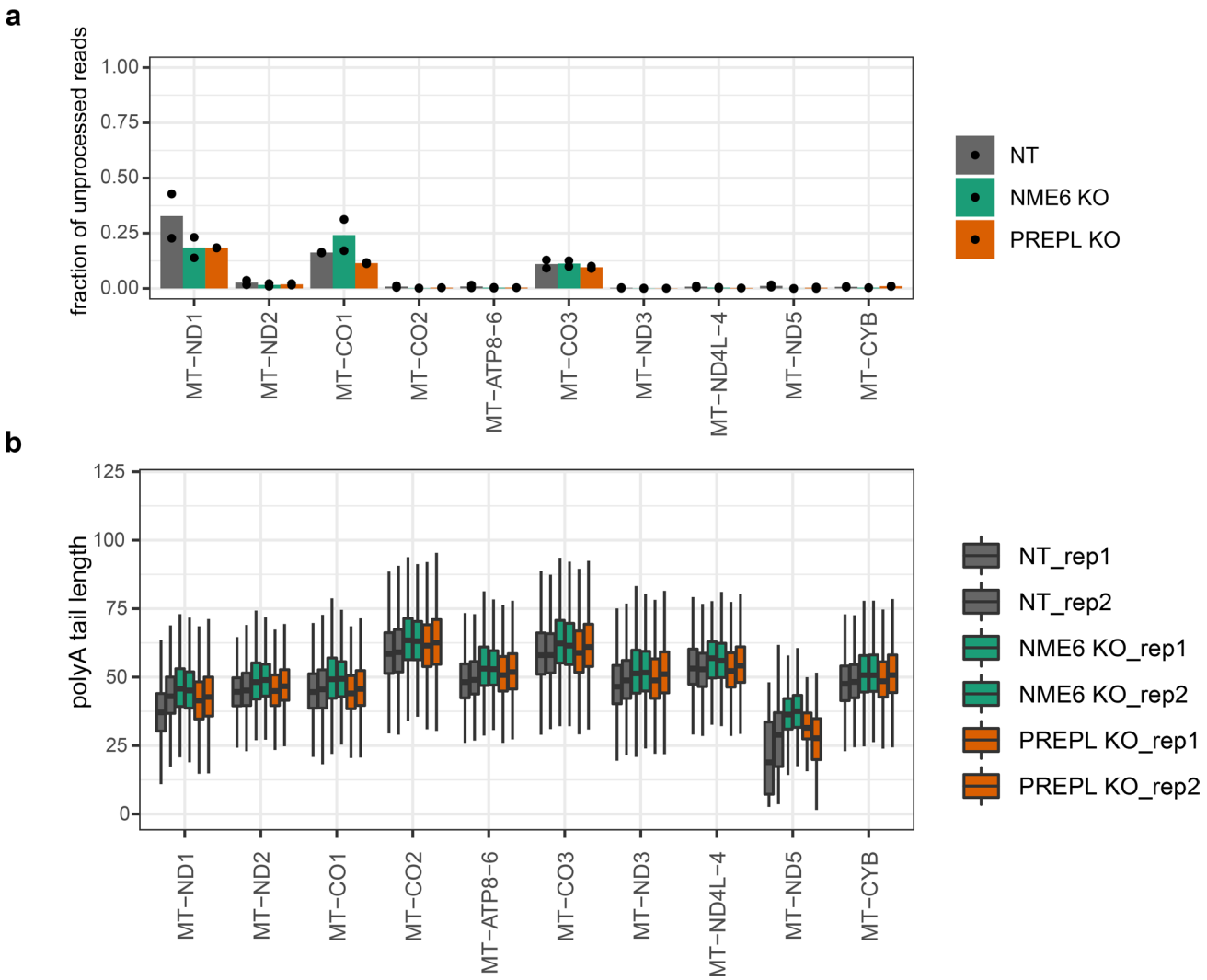

Extended Data Fig. 5 | Direct RNA nanopore sequencing in control (NT), PREPL KO and NME6 KO cells. (**a**) Measurement of 5′-end processing levels for mt-mRNAs encoded on the heavy strand and (**b**) poly(A) tail lengths of mt-mRNAs in control, NME6 KO and PREPL KO cells. n = 2 biological replicate samples sequenced independently, shown as dots in (**a**) and side-by-side in (**b**). Box plots: center line, median; box limits, upper and lower quartiles; whiskers, 1.5 × interquartile range. Source numerical data are available in source data.

https://doi.org/10.1038/s41556-023-01244-3

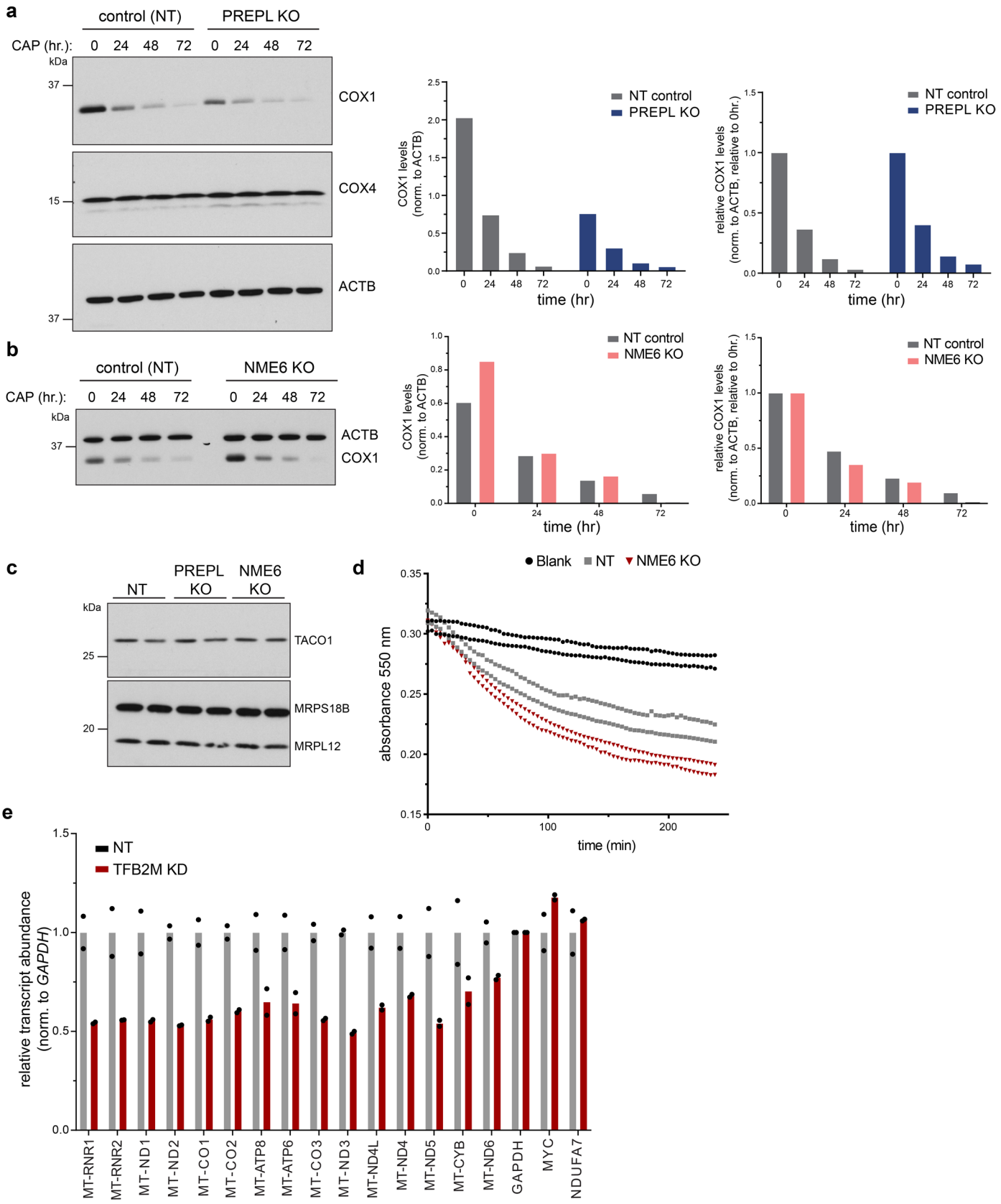

Extended Data Fig. 6 | See next page for caption.

https://doi.org/10.1038/s41556-023-01244-3

Extended Data Fig. 6 | Mitochondrial protein turnover assays in (**a**) PREPL KO cells or (**b**) NME6 KO cells. Left panels: Cells were pulsed with 200 μg ml^{-1} CAP to inhibit new mitochondrial protein synthesis for 0, 24 hr, 48 hr, or 72 hr., and proteins were detected via western blotting. Right panels: Quantifications of COX1 bands by densitometry were normalized to ACTB levels and plotted directly or normalized to time = 0 time points for each genotype to correct for the steady-state subunit abundance levels in PREPL or NME6 KO cells. Representative blots from 2 independent experiments. (**c**) Western blot analysis of TACO1 levels in PREPL KO or NME6 KO cells, MRPS18B and MRPL12 were used for loading controls. Representative blots from 2 independent experiments. (**d**) Complex IV enzymatic activity measured colorimetrically by monitoring the oxidation of reduced cytochrome *c* over time from mitochondrial lysates immunocaptured on microplate wells coated with anti-Complex IV antibodies (n = 2 independent biological replicate lysates; related to Fig. 5j). Shown here are the activities for 10 μg mitochondrial protein added per well in control and NME6 KO cells. Activities in OD/min were determined for Fig. 5j by calculating the slope between 2 time points within the linear range of activity. (**e**) MitoStrings quantifications of RNA transcript abundance in control (NT) or *TFB2M* pooled CRISPR knock-down cells (bar plots represent the means of the replicates, n = 2 independent cultures). Source numerical data and unprocessed blots are available in source data.

https://doi.org/10.1038/s41556-023-01244-3

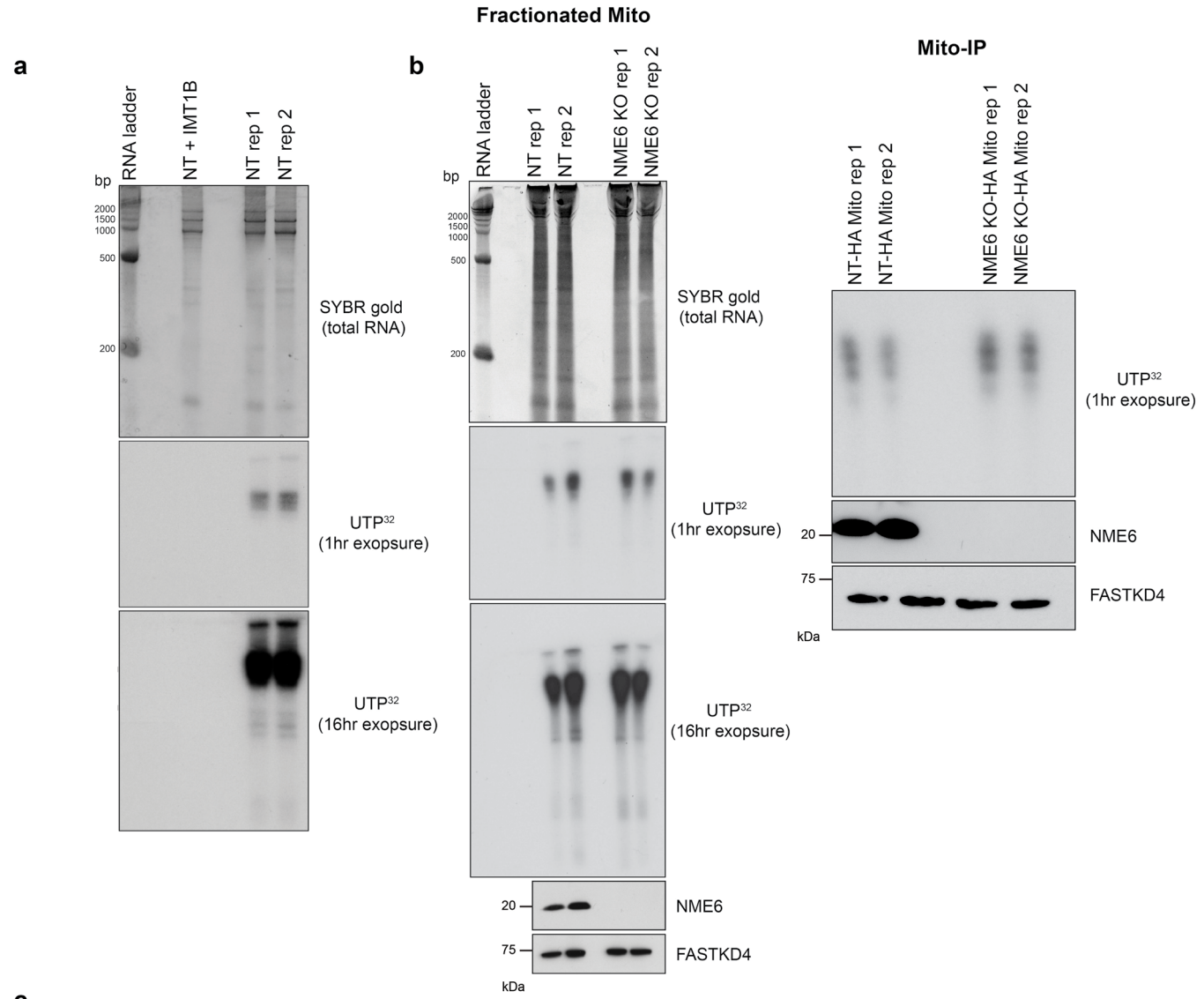

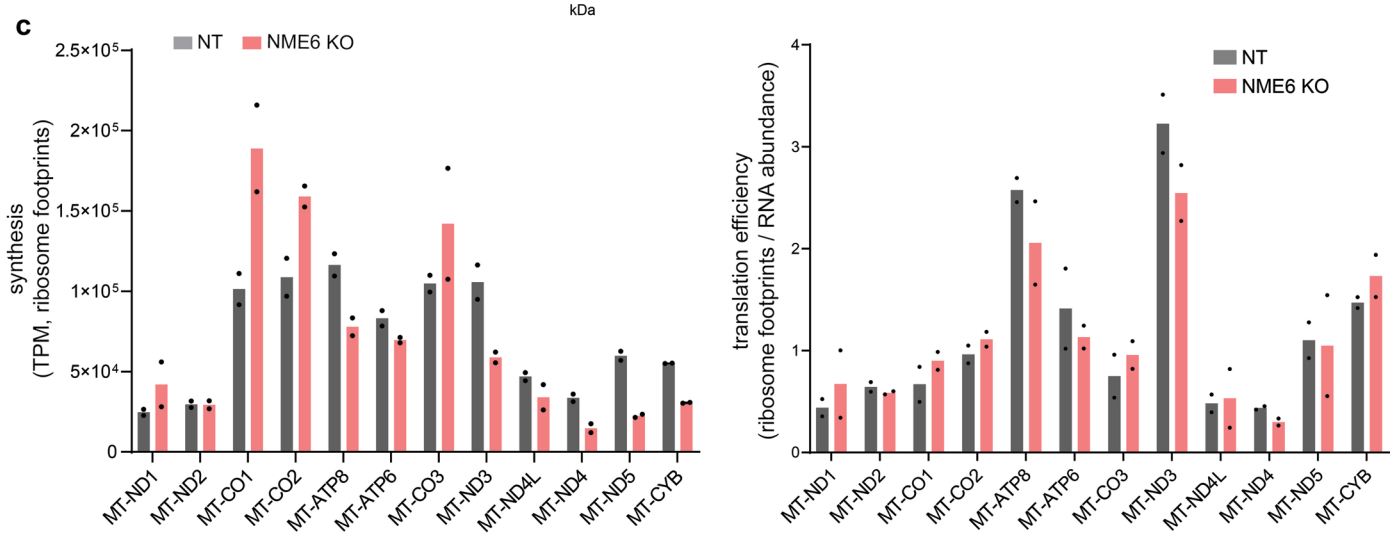

Extended Data Fig. 7 | *In organello* mitochondrial transcription visualized by ^{32}P-UTP labelling in purified mitochondria. RNA was visualized using TBE-urea PAGE, followed by autoradiography of newly synthesized mtRNA. SYBR gold staining of total RNA and western blots on input mitochondrial lysates were included for controls. (**a**) IMT1B was used as a positive control to inhibit mitochondrial transcription in NT control cells (5uM, 2 hr. pre-treatment in culture and maintained in labelling reaction). Representative gels from 3 independent experiments. (**b**) Transcription assays from fractionated or mt-IP purified mitochondria in NT and NME6 KO cells. Representative gels from 2 independent experiments. (**c**) Left, ribosome profiling analysis plotting synthesis (TPM = transcript per million) using mitoribosome protected footprints mapped to mitochondrial RNAs and Right, translation efficiency (ribosome footprints normalized by total RNA abundance; n = 2 independently sequenced libraries; related to Fig. 8c). Source numerical data and unprocessed blots are available in source data.

https://doi.org/10.1038/s41556-023-01244-3

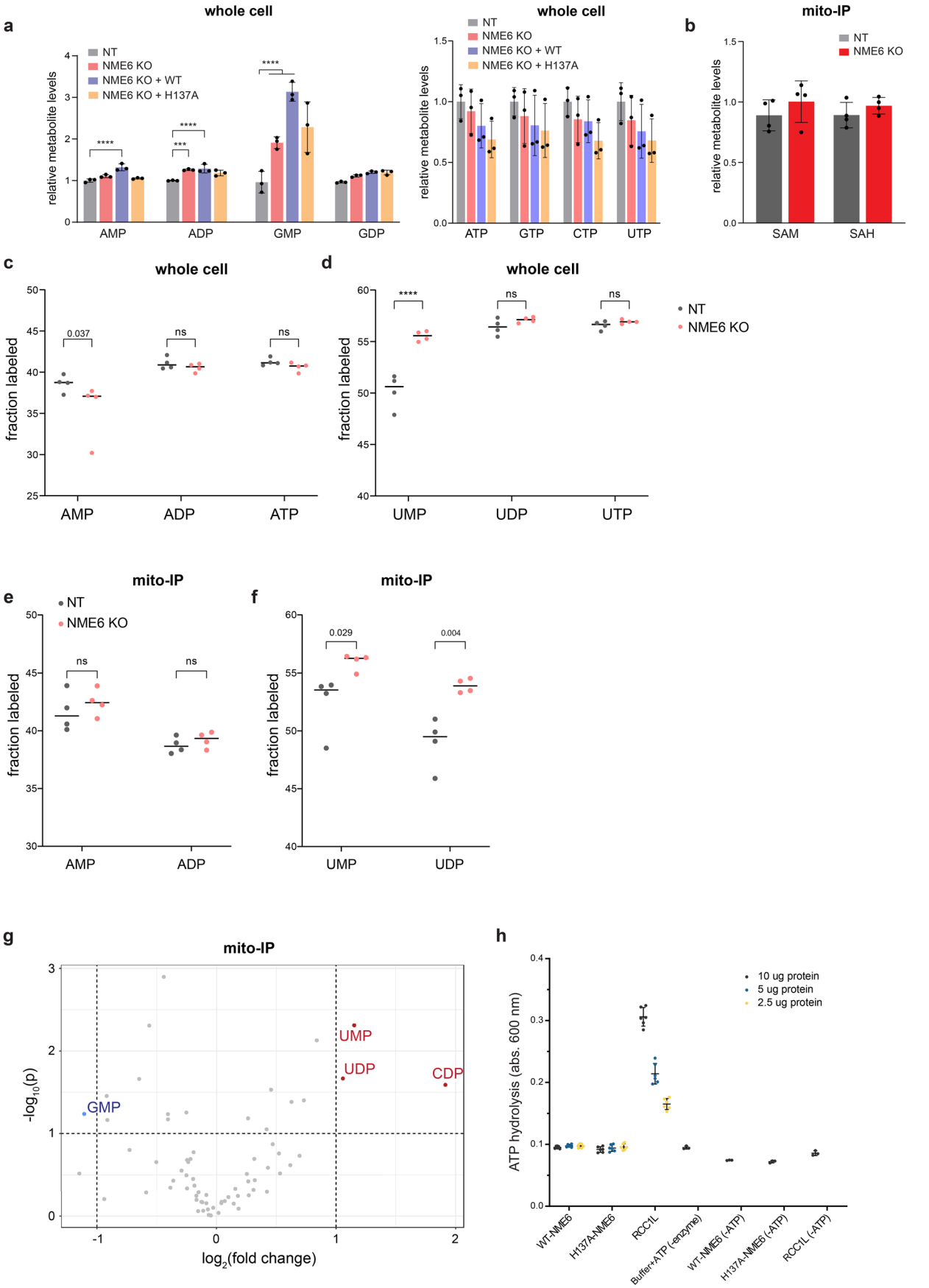

Extended Data Fig. 8 | See next page for caption.

https://doi.org/10.1038/s41556-023-01244-3

Extended Data Fig. 8 | (**a**) Metabolite levels quantified by mass spectrometry in whole cell extractions from NT, NME6 KO, and WT/H137A rescue cell lines (relative to NT; n = 3 independent cultures; two-way ANOVA with Dunnett's multiple comparisons correction, *** p = 0.0001, **** p < 0.0001, data are means +/− SD). (**b**) Metabolite levels in NT or NME6 KO mt-IP cell lines after HA-IP (relative to NT; n = 4 independent cultures; data are means +/− SD). SAM = S-adenosylmethionine, SAH = S-adenosylhomocysteine. (**c-f**) Isotope tracing using 13C-labelled glucose (22 hr. labelling) and mass spectrometry detection of labelling efficiency for plotted metabolites (c-d = whole cell lysates, e-f = mt-IP lysates; n = 4 independent cultures, two-way ANOVA with Sidak's multiple comparisons correction, **** p < 0.0001). (**g**) Volcano plot for all confidently detected metabolites in mt-IP extracts comparing fold change in metabolites (NME6 KO/NT) vs significance values (two-tailed t-test with FDR correction). (**h**) Malachite green phosphate assay showing background control values for data presented in Fig. 7e. Data are means +/− SD. Source numerical data are available in source data.

https://doi.org/10.1038/s41556-023-01244-3

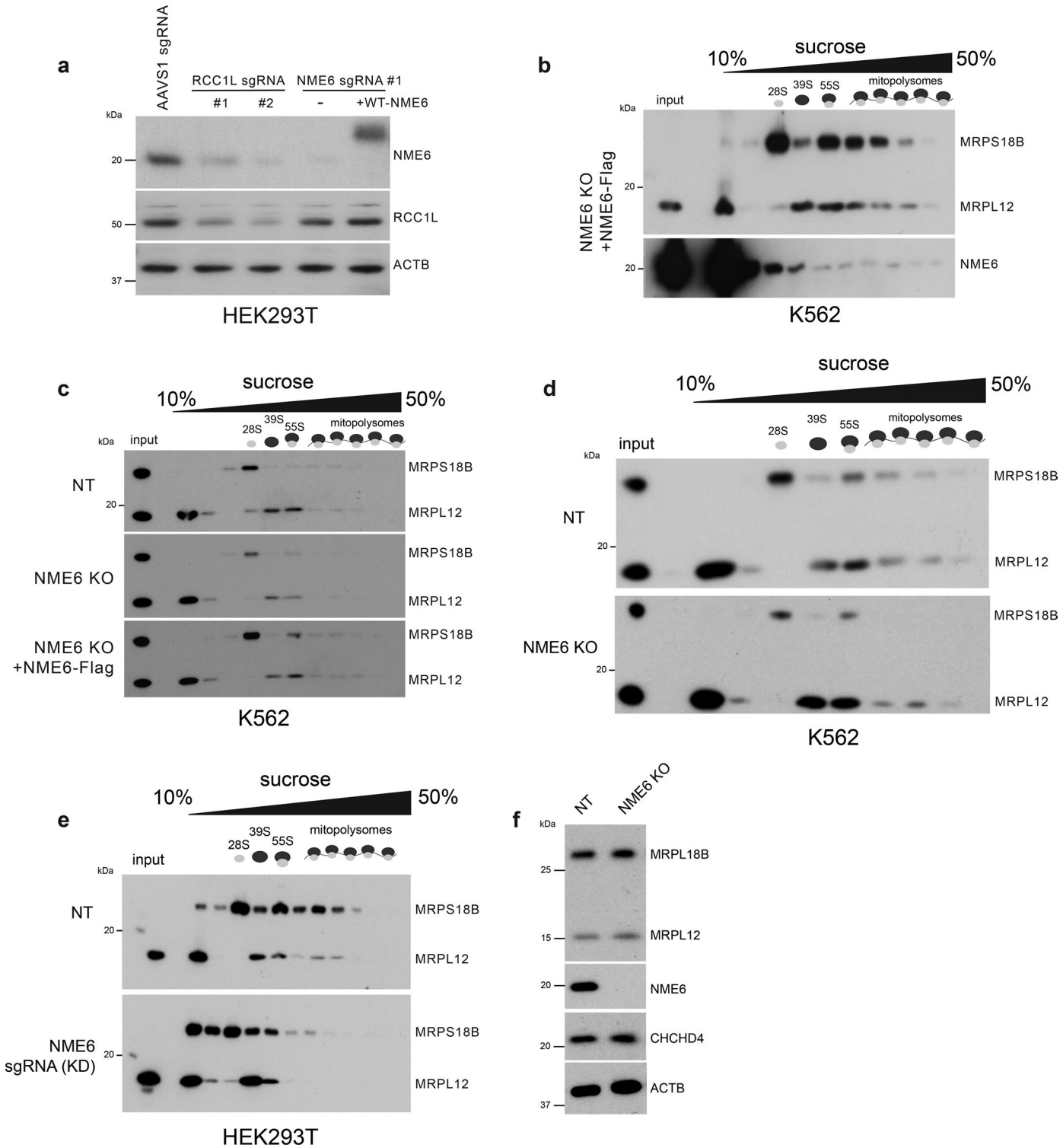

Extended Data Fig. 9 | (**a**) Western blot analysis of HEK293T cells transduced with indicated sgRNAs (AAVS1 = control sgRNA). (**b**-**e**) Sucrose gradient centrifugation and fractionation followed by western blotting. (**b**) NME6 co-sedimentation with mitoribosomes in K562 cells expressing NME6-Flag. (**c**-**e**) Mitoribosome assembly phenotypes detected by western blotting after sucrose gradient centrifugation and fractionation using antibodies for small (MRPS18B) and large (MRPL12) mitoribosome subunits to monitor mitoribosome assembly in (**c**, **d**) NME6 KO K562 cells and (**e**) NME6 sgRNA-transduced pooled knock-down (KD) HEK293T cells. (**f**) Western blot analysis of steady-state mitoribosome subunit levels in control (NT) and NME6 KO cells. All experiments repeated at least twice independently. Unprocessed blots are available in source data.

https://doi.org/10.1038/s41556-023-01244-3

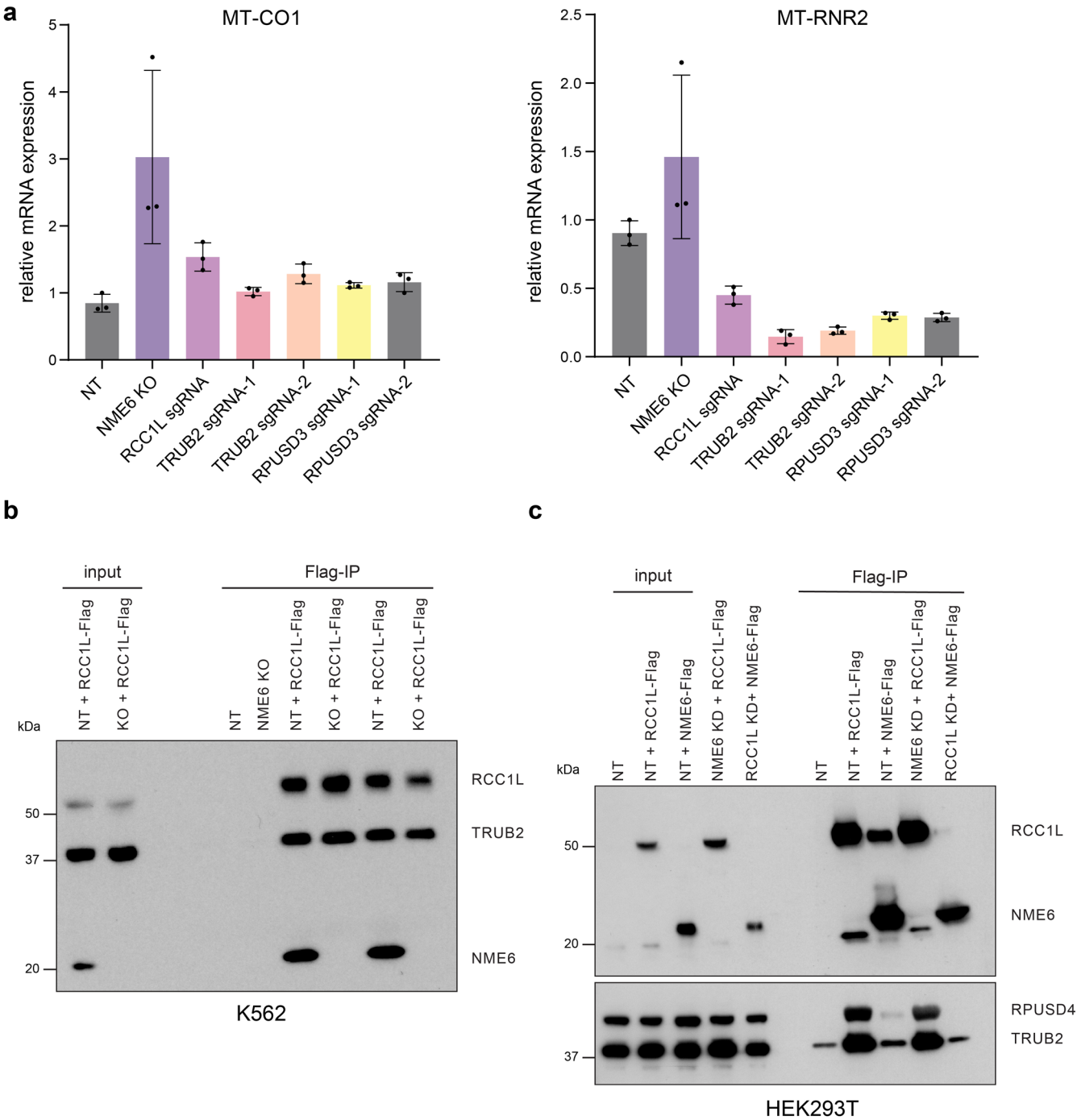

Extended Data Fig. 10 | (**a**) qRT-PCR for *MT-CO1* levels (left) or *MT-RNR2* levels (right) in NT (control), NME6 KO, or K562 pooled CRISPR knock-down cells with the indicated sgRNAs targeting TRUB2, RCC1L, or RPUSD3 (n = 3 independent replicates for each sgRNA, data are means −/+ SD). (**b, c**) Western blot analysis of RCC1L-Flag IPs in NT (control) or NME6 KO cell backgrounds in K562 and HEK293T, respectively. Representative blots from 2 independent experiments. Source numerical data and unprocessed blots are available in source data.

nature portfolio

Corresponding author(s): L. Stirling Churchman

Last updated by author(s): Aug 21, 2023

Reporting Summary

Nature Portfolio wishes to improve the reproducibility of the work that we publish. This form provides structure for consistency and transparency in reporting. For further information on Nature Portfolio policies, see our Editorial Policies and the Editorial Policy Checklist.

Statistics

For all statistical analyses, confirm that the following items are present in the figure legend, table legend, main text, or Methods section.

n/a	Confirmed	
☐	☒	The exact sample size (*n*) for each experimental group/condition, given as a discrete number and unit of measurement
☐	☒	A statement on whether measurements were taken from distinct samples or whether the same sample was measured repeatedly
☐	☒	The statistical test(s) used AND whether they are one- or two-sided *Only common tests should be described solely by name; describe more complex techniques in the Methods section.*
☐	☒	A description of all covariates tested
☐	☒	A description of any assumptions or corrections, such as tests of normality and adjustment for multiple comparisons
☐	☒	A full description of the statistical parameters including central tendency (e.g. means) or other basic estimates (e.g. regression coefficient) AND variation (e.g. standard deviation) or associated estimates of uncertainty (e.g. confidence intervals)
☐	☒	For null hypothesis testing, the test statistic (e.g. *F*, *t*, *r*) with confidence intervals, effect sizes, degrees of freedom and *P* value noted *Give P values as exact values whenever suitable.*
☒	☐	For Bayesian analysis, information on the choice of priors and Markov chain Monte Carlo settings
☒	☐	For hierarchical and complex designs, identification of the appropriate level for tests and full reporting of outcomes
☒	☐	Estimates of effect sizes (e.g. Cohen's *d*, Pearson's *r*), indicating how they were calculated

Our web collection on statistics for biologists contains articles on many of the points above.

Software and code

Policy information about availability of computer code

Data collection	Metabolomics data collection: TraceFinder 5.1 (Thermo Fisher Scientific)
Data analysis	Metabolomics data analysis: https://github.com/FrozenGas/KanarekLabTraceFinderRScripts/blob/main/MS_data_script_v2.4_20221018.R CRISPR screen analysis performed with published softward: MAGeCK (https://sourceforge.net/p/mageck/wiki/Home/) and casTLE (https://github.com/elifesciences-publications/dmorgens-castle) CMC-sequencing was analyzed using custom scripts from: PMID: 27974379 Flow cytometry data were all analyzed with commercially available software: FlowJo v10.8.1 Long read Nanopore sequencing: MinKNOW v20.10.3, minimap2 v2.25

For manuscripts utilizing custom algorithms or software that are central to the research but not yet described in published literature, software must be made available to editors and reviewers. We strongly encourage code deposition in a community repository (e.g. GitHub). See the Nature Portfolio guidelines for submitting code & software for further information.

Data

Policy information about availability of data

All manuscripts must include a data availability statement. This statement should provide the following information, where applicable:

- Accession codes, unique identifiers, or web links for publicly available datasets
- A description of any restrictions on data availability
- For clinical datasets or third party data, please ensure that the statement adheres to our policy

Data availability statement in manuscript: Deep-sequencing data that support the findings of this study have been deposited in the Gene Expression Omnibus (GEO) under accession codes GSE224819. Mass spectrometry data have been deposited with ProteomeXchange (PRIDE) with the primary accession code PXD044812. Metabolomics data are available in Supplemental Table 3. Numerical source data and unprocessed blots are available in Source Data. All other data supporting the findings of this study are available from the corresponding author on reasonable request.

Human research participants

Policy information about studies involving human research participants and Sex and Gender in Research.

Reporting on sex and gender	N/A
Population characteristics	N/A
Recruitment	N/A
Ethics oversight	N/A

Note that full information on the approval of the study protocol must also be provided in the manuscript.

Field-specific reporting

Please select the one below that is the best fit for your research. If you are not sure, read the appropriate sections before making your selection.

☒ Life sciences ☐ Behavioural & social sciences ☐ Ecological, evolutionary & environmental sciences

For a reference copy of the document with all sections, see nature.com/documents/nr-reporting-summary-flat.pdf

Life sciences study design

All studies must disclose on these points even when the disclosure is negative.

Sample size	Sample size determination not performed but is representative of numbers used throughout the field.
Data exclusions	No data exclusion performed
Replication	Experiments were replicated as described in the relevant figure legends or methods sections. Genome-wide screens were independently performed twice.
Randomization	Randomization not relevant to our study and was not performed. Our experimental methods are not impacted by randomization.
Blinding	Bliding not relevant to our study and was not performed. Our experimental methods are not impacted by blinding.

Reporting for specific materials, systems and methods

We require information from authors about some types of materials, experimental systems and methods used in many studies. Here, indicate whether each material, system or method listed is relevant to your study. If you are not sure if a list item applies to your research, read the appropriate section before selecting a response.

Materials & experimental systems

n/a	Involved in the study
☐	☒ Antibodies
☐	☒ Eukaryotic cell lines
☒	☐ Palaeontology and archaeology
☐	☒ Animals and other organisms
☒	☐ Clinical data
☒	☐ Dual use research of concern

Methods

n/a	Involved in the study
☒	☐ ChIP-seq
☐	☒ Flow cytometry
☒	☐ MRI-based neuroimaging

Antibodies

Antibodies used

MT-CO1/COX1 (ABCAM, ab14705, 1:2000), COX4I1/COX4 (CST, 4850, 1:1000), ACTB (CST, 3700, 1:5000), FLAG (Millipore Sigma, F1804,1:5000), LRPPRC (Abcam, Ab97505, 1:1000), TOMM40 (Proteintech, 18409-1-AP,1:5000), MRPS18B (Proteintech, 16139-1-AP,1:1000), MRPL12 (Proteintech, 14795-1-AP,1:750), WBSCR16/RCC1L (Proteintech, 13796-1-AP, 1:1000), NDUFS1 (Abcam, ab169540,1:1000), SDHA (Santa Cruz, sc-166947,1:10,000), UQCR4/CYC1 (Millipore Sigma, HPA001247,1:1000), MT-ATP6 (ProteinTech, 55313-1-AP,1:1000), ATP5H (Abcam, ab110275,1:1000), MT-ND1 (Abcam, ab181848,1:1000), MT-CYB (ProteinTech, 55090-1-AP,1:1000), NME6 (Millipore Sigma, HPA017909,1:1000), PREPL (Abcam, ab202064,1:1000), CHCHD4 (ProteinTech 21090-1-AP,1:1000), TRUB2 (ProteinTech,19891-1-AP, 1:1000), RPUSD4 (Millipore Sigma HPA039689,1:1000), TBRG4 (Sigma , HPA020582,1:1000), GAPDH (Invitrogen, A5-15738,1:1000), TFAM (sc-376672,1:2000) and TACO1 (ProteinTech, 21147-1-AP, 1:1000).

Validation

MT-CO1, COX4I1, PREPL, NME6, RCC1L, TACO1 primary antibodies all validated for human targets by knockdown, overexpression, or pharmacological inhibition in this manuscript. All other antibodies used as indicated according to validation data provided by the manufacturer in their respective websites.

Eukaryotic cell lines

Policy information about cell lines and Sex and Gender in Research

Cell line source(s)	K562, U2OS and HEK293T cells were purchased from ATCC
Authentication	Cell lines not authenticated
Mycoplasma contamination	Cell lines tested negative for mycoplasma
Commonly misidentified lines (See ICLAC register)	None

Animals and other research organisms

Policy information about studies involving animals; ARRIVE guidelines recommended for reporting animal research, and Sex and Gender in Research

Laboratory animals	8-week old, male C57BL/6 (Charles River, C57BL/6NCrl) mice were used for tissue collection where indicated.
Wild animals	N/A
Reporting on sex	*Indicate if findings apply to only one sex; describe whether sex was considered in study design, methods used for assigning sex. Provide data disaggregated for sex where this information has been collected in the source data as appropriate; provide overall numbers in this Reporting Summary. Please state if this information has not been collected. Report sex-based analyses where performed, justify reasons for lack of sex-based analysis.*
Field-collected samples	N/A
Ethics oversight	Harvard University IACUC approved protocol

Note that full information on the approval of the study protocol must also be provided in the manuscript.

Flow Cytometry

Plots

Confirm that:

☒ The axis labels state the marker and fluorochrome used (e.g. CD4-FITC).

☒ The axis scales are clearly visible. Include numbers along axes only for bottom left plot of group (a 'group' is an analysis of identical markers).

☒ All plots are contour plots with outliers or pseudocolor plots.

☒ A numerical value for number of cells or percentage (with statistics) is provided.

Methodology

Sample preparation	Methanol fixation and permeabilization of cultured K562 cells
Instrument	Sony SH800Z flow cytometer (sorter) or LSRII (analyzer)
Software	FlowJo (BD) v10.8.1
Cell population abundance	FACS was performed on K562 cell lines, so purity is not applicable here.
Gating strategy	FSC/SSC was used to exclude dead cells/debris, singlets were enriched by FSC-A vs FSC-H before gating on immunostained cells of interest. Negative/positive populations were determined by combinations of unstained and single stained controls.

☒ Tick this box to confirm that a figure exemplifying the gating strategy is provided in the Supplementary Information.